FORSCHUNGSZENTRUM KARLSRUHE

Technik und Umwelt

Wissenschaftliche Berichte

FZKA 5967

# STELLAR NEUTRON CAPTURE CROSS SECTIONS OF THE Nd ISOTOPES

K. WISSHAK, F. VOSS, F. KÄPPELER, L. KAZAKOV[1], and G. REFFO[2]

Institut für Kernphysik

[1]Institute for Physics and Power Engineering, Obninsk, Kaluga Region, Russia
[2]ENEA, Centro Dati Nucleari, Via Martiri di Monte Sole 4, I–40138 Bologna, Italy

Forschungszentrum Karlsruhe GmbH, Karlsruhe
1997

# ABSTRACT

The neutron capture cross sections of $^{142}$Nd, $^{143}$Nd, $^{144}$Nd, $^{145}$Nd, $^{146}$Nd, and $^{148}$Nd have been measured in the energy range from 3 to 225 keV at the Karlsruhe 3.75 MV Van de Graaff accelerator. Neutrons were produced via the $^{7}$Li(p,n)$^{7}$Be reaction by bombarding metallic Li targets with a pulsed proton beam. Capture events were registered with the Karlsruhe $4\pi$ Barium Fluoride Detector. The cross sections were determined relative to the gold standard. The experiment was difficult due to the small cross sections of the even isotopes at or near the magic neutron number N=82, and also since the isotopic enrichment of some samples was comparably low. The necessary corrections for capture of scattered neutrons and for isotopic impurities could be determined reliably thanks to the high efficiency and the spectroscopic quality of the $BaF_2$ detector, resulting in a consistent set of (n,$\gamma$) cross sections for the six stable neodymium isotopes involved in the s–process with typical uncertainties of 1.5–2%. From these data, Maxwellian averaged cross sections were calculated between kT = 10 keV and 100 keV. The astrophysical implications of these results were investigated in an s–process analysis based on the classical approach, which deals with the role of the s–only isotope $^{142}$Nd for the $N_s<\sigma>$–systematics near the magic neutron number N=82, the decomposition of the Nd abundances into the respective r– , s–, and p–process components, and the interpretation of isotopic anomalies in meteoritic material.

# ZUSAMMENFASSUNG

## DIE STELLAREN (n,$\gamma$) QUERSCHNITTE DER Nd ISOTOPE

Am Karlsruher Van de Graaff Beschleuniger wurden die Neutroneneinfangquerschnitte von $^{142}$Nd, $^{143}$Nd, $^{144}$Nd, $^{145}$Nd, $^{146}$Nd und $^{148}$Nd im Energiebereich von 3 bis 225 keV relativ zu Gold als Standard bestimmt. Neutronen wurden über die $^{7}$Li(p,n)$^{7}$Be–Reaktion durch Beschuß metallischer Li–Targets mit einem gepulsten Protonenstrahl erzeugt. Einfangereignisse wurden mit dem Karlsruher $4\pi$ Barium–Fluorid–Detektor nachgewiesen. Das Experiment wurde durch die kleinen Einfangquerschnitte in der Nähe der magischen Neutronenzahl N=82 und durch die relativ schwache Isotopenanreicherung einiger Proben erschwert. Die dadurch bedingten Korrekturen für Untergrund durch gestreute Neutronen und für Fremdisotope ließen sich jedoch aufgrund der hohen Nachweiswahrscheinlichkeit und der spektroskopischen Qualität des $BaF_2$–Detektors zuverlässig ermitteln. Auf diese Weise konnte für die sechs am s–Prozeß beteiligten, stabilen Neodymisotope ein konsistenter Satz von (n,$\gamma$)–Querschnitten mit typischen Unsicherheiten von 1.5–2% bestimmt werden. Aus diesen Daten wurden maxwellgemittelte Querschnitte zwischen kT = 10 keV und 100 keV berechnet. Die Konsequenzen dieser Ergebnisse für die Nukleosynthese im s-Prozeß wurde auf der Grundlage der klassischen Näherung untersucht, insbesondes im Hinblick auf die Rolle des reinen s–Kerns $^{142}$Nd für die $N_s<\sigma>$–Systematik bei der magischen Neutronenzahl N=82, die Zerlegung der Nd–Häufigkeiten in die jeweiligen r– , s–, and p–Prozeß–Anteile und die Interpretation von Isotopenanomalien in meteoritischem Material.

# Contents

# 1 INTRODUCTION

In s–process nucleosynthesis, the neutron capture cross sections of the neodymium isotopes are important for the following reasons:

- $^{142}$Nd is an s–only isotope located immediately at the pronounced precipice of the $N_s<\sigma>$curve caused by the small (n,$\gamma$) cross sections at magic neutron number N=82. This precipice is critically determined by the mean neutron exposure of the main s–process component, $\tau_0$ [1]. Thus $^{142}$Nd complements the common normalization points $^{124}$Te and $^{150}$Sm and represents an additional constraint for the determination of $\tau_0$.

- As indicated in Fig.1, there are weak s-process branchings at $^{141}$Ce and $^{142}$Pr. According to Ref.[2] about 5% of the synthesis flow is bypassing $^{142}$Nd. These branchings are not sensitive to stellar temperatures [3] and can be analysed using the neutron density derived from other branchings [4]. In this way, the small but significant s component of the $^{142}$Ce abundance can be determined for this isotope which was previously considered to be of pure r-process origin.

- Reliable cross sections for the isotopes involved in the branchings at A=141/142 are required for an improved estimate for the p–process abundance of $^{142}$Nd. The previously recommended $^{142}$Nd cross section yields an empirical $N_s<\sigma>$–value significantly above the $N_s<\sigma>$–curve [2], indicating a p–process component of almost 20% much larger than predicted by recent p-process calculations [5, 6, 7]. A lower cross section of $^{142}$Nd would imply an increase of the s– and a corresponding reduction of the p-process component. A quantitative determination of the p–process yield for $^{142}$Nd is of interest with respect to the enhanced feeding via the comparably short–lived $\alpha$–decay chain $^{154}$Dy–$^{150}$Gd–$^{146}$Sm–$^{142}$Nd [8].

- Accurate cross sections for all neodymium isotopes will allow for an improved separation between r and s abundances in this mass region since the existing data show severe discrepancies. Presently, the r–process abundance pattern exhibits pronounced odd–even differences between A=140 and 150 [9] in contrast to an expected smooth behavior, which may reflect the problems in determining the small cross sections of the even isotopes. For example, the r–residuals of the neighboring isotopes $^{146}$Nd and $^{147}$Sm differ by a factor of three [1]. This mass region right above the r–abundance peak at A=130 is crucial for comparison with recent r–process calculations [10, 11]. An improved r– and s–process separation of the neodymium abundances is also of interest for discussing the Nd/Th ratio as a possible cosmochronometer [12, 13].

- The discovery of strong isotopic anomalies in neodymium can be interpreted as pure s–process material [14, 15]. However, a discussion based on the older cross sections led to significant inconsistencies. Therefore, it was suggested that this problem could be solved by a modification of the neodymium cross sections, in particular of that for $^{144}$Nd [4, 64].

The experimental situation for the neodymium isotopes is quite peculiar. On average, six measurements were reported for these nuclei [17, 18], which means that neodymium is among the most frequently investigated elements. Nevertheless, the individual results differ by factors of two to three in all cases. The present experiment aims, therefore, at a significant improvement of the stellar (n,$\gamma$) cross sections for all neodymium isotopes as an essential prerequisite for detailed s–process analyses.

Figure 1: The s–process paths in the region of the neodymium isotopes.

The measurement of these cross sections must account for three complications:

- The (n,$\gamma$) cross sections of the even isotopes near the magic neutron number N=82, in particular of $^{142}$Nd, are fairly small. This implies large scattering-to-capture ratios which were further increased by the fact that the samples had to be prepared from neodymium oxide. Accordingly, sizable corrections for capture of scattered neutrons were unavoidable.

- For some isotopes, the available enrichment was only 70% – 80%. The cross sections of neighboring isotopes being very different results in large corrections already for isotopic impurities of a few percent. For example, the cross sections of $^{142}$Nd and $^{143}$Nd differ by a factor of eight.

- Neodymium oxide can be very hygroscopic. This trivial point was not sufficiently considered in the past and may well account for the large discrepancies among the older data.

While the first two items are difficult to handle with conventional TOF methods, the present setup is well suited for treating both corrections properly. This was demonstrated at the more extreme examples of the barium isotopes [19], where the background due to capture of scattered neutrons was even larger, and of the gadolinium isotopes [20] where the corrections for isotopic impurities were also larger than in the present case. The third point emphasizes that sample preparation and characterization has to be performed with greatest care.

Measurement and data analysis are described in Secs. 2 and 3, followed by a discussion of the results in Sec. 4, and of the uncertainies in Sec. 5. The stellar cross sections are presented in Sec. 6. Finally, the astrophysical implications are outlined in Sec.7.

# 2 EXPERIMENT

## 2.1 Experimental Method

The neutron capture cross sections of the neodymium isotopes 142 to 146 and 148 have been measured in the energy range from 3 to 225 keV using gold as a standard. Since the experimental method has been published in detail [21, 22, 23, 24], only a more general description is given here, complemented with the specific features of the present measurement.

Neutrons were produced via the $^7$Li(p,n)$^7$Be reaction by bombarding metallic Li targets with the pulsed proton beam of the Karlsruhe 3.75 MV Van de Graaff accelerator. The neutron energy was determined by time of flight (TOF), the samples being located at a flight path of 79 cm. The important parameters of the accelerator were a pulse width of $<$1 ns, a repetition rate of 250 kHz, and an average beam current of 1.5 $\mu$A. In different runs, the proton energies were adjusted 30 and 100 keV above the threshold of the $^7$Li(p,n)$^7$Be reaction at 1.881 MeV. In this way, continuous neutron spectra in the energy range of interest for s–process studies were obtained, ranging from 3 to 100 keV, and 3 to 200 keV, respectively. The lower maximum neutron energy offers a significantly better signal to background ratio at lower energies.

Capture events were registered with the Karlsruhe 4$\pi$ Barium Fluoride Detector via the prompt capture $\gamma$–ray cascades. This detector consists of 42 hexagonal and pentagonal crystals forming a spherical shell of $BaF_2$ with 10 cm inner radius and 15 cm thickness. It is characterized by a resolution in $\gamma$–ray energy of 7% at 2.5 MeV, a time resolution of 500 ps, and a peak efficiency of 90% at 1 MeV. The threshold for the detection of capture events was 1.4 MeV which yields an efficiency for capture events of more than 97% for all neodymium isotopes despite the comparably low binding energies. For a comprehensive description see Ref. [23].

The experiment was divided into four runs, two with the conventional data acquisition technique with the detector operated as a calorimeter, and two with an ADC system

coupled to the detector for analyzing the signals from all modules individually. In this way, the full spectroscopic information recorded by the detector can be recovered.

## 2.2 Samples

The samples were prepared from isotopically enriched neodymium oxide ($Nd_2O_3$). Special precautions were taken to eliminate any water by heating to 1200 K for 15 min. Then, the oxide was pulverized in an agate mortar to obtain the fine powder which was used for pressing pellets of 22 mm diameter. These pellets shrinked slightly when they were again heated to 1200 K for one hour. Immediately after cooling, the final samples were prepared by enclosing the pellets into cylindrical aluminum cannings with 0.2 mm thick walls.

During this procedure the sample weight was continuously controlled. After the first heating the different batches of separated isotopes lost between 2.5% and 15% of their weight. In the second heating any further losses from the stable pellets were below 0.5%. As a consequence of the extreme water content of 15% the sample would have contained three times more hydrogen than neodymium atoms! The scattering cross section of hydrogen being only a factor of two smaller than of neodymium would have caused significant neutron moderation and, hence, a strongly enhanced probability for capture of scattered neutrons. This effect is proportional to the sample mass and inversely proportional to the cross section, and would, therefore, affect mainly the even isotopes where larger samples are required and where the primary capture probability is low. As illustrated by Mizumoto and Sugimoto [25] this can easily lead to a "cross section excess" of a factor of two.

The problem with absorbed water has been discussed already for the rare earth elements samarium and gadolinium [20, 22], but was most crucial in the present case. While samarium and gadolinium pellets turned out to be very stable after heating and could easily be stored in air, three of the neodymium samples had to be reprocessed during the first run because water had accumulated through small leaks in the aluminum canning. After careful inspection of the new aluminium cans, the sample weight remained constant during the first three runs of the experiment. Before Run IV, however, which started about 16 weeks after the end of Run III, four of the six samples were freshly processed because an increase in weight had been detected. For comparison, pellets prepared under identical conditions from ordinary neodymium oxide but stored in air without canning showed quite irregular behavior. Some of these samples were destroyed within a few days, others remained stable over four weeks but decayed then suddenly into powder within only one or two days.

The relevant parameters of the samples are compiled in Table 1. In addition to the six enriched neodymium samples, a gold sample in an identical Al canning was used. The background due to scattered neutrons was simulated by a $^{208}$Pb sample as well as by a graphite sample. This allowed to study experimentally whether the slightly different energy losses in the scattering process and the related TOF shift of the scattered neutrons may affect this correction. An empty canning was installed in an additional position of the sample ladder for determining the sample-independent background. Losses in reprocessing the samples were always well below 1% and and were considered in data evaluation.

Table 1: SAMPLE CHARACTERISTICS

| Sample | Diameter | Thickness | | Weight[1] | Canning[2] | Neutron binding energy |
|---|---|---|---|---|---|---|
| | (mm) | (mm) | ($10^{-3}$at/barn)[3] | (g) | (g) | (MeV) |
| $^{142}$Nd | 20.94 | 4.74 | 6.6374 | 6.9587 | 0.5879 | 6.123 |
| $^{208}$Pb[4] | 22.06 | 1.84 | 5.8196 | 7.6396 | 0.5420 | |
| $^{143}$Nd | 21.87 | 1.83 | 2.9768 | 3.1426 | 0.5535 | 7.817 |
| $^{145}$Nd | 19.51 | 1.16 | 1.5294 | 1.6323 | 0.5291 | 7.565 |
| $^{197}$Au | 22.02 | 0.26 | 1.5048 | 1.8709 | 0.5314 | 6.513 |
| $^{146}$Nd | 21.24 | 3.32 | 4.7405 | 5.0849 | 0.5482 | 5.292 |
| $^{148}$Nd | 21.87 | 2.41 | 3.6263 | 3.9255 | 0.5711 | 5.039 |
| Empty | | | | | 0.5540 | |
| $^{144}$Nd | 21.39 | 4.56 | 7.0125 | 7.4371 | 0.6939 | 5.756 |
| Graphite[5] | 22.08 | 1.41 | 11.9041 | 0.9091 | 0.5300 | |

[1]For neodymium samples: weight of $Nd_2O_3$
[2]Aluminum cylinder
[3]For neodymium samples: sum of all Nd isotopes
[4]Used in Runs I and II
[5]Used in Runs III and IV

The isotopic compositions provided by the supplier are listed in Table 2. Originally, uncertainties were not specified, but were determined in an additional analysis at IPPE Obninsk after the experiment. The composition of the two most important samples enriched in $^{142}$Nd and $^{144}$Nd was measured at FZK Karlsruhe, as well. These results are summarized in Table 2.

The neutron transmission of the samples was calculated with the SESH code [26], and was generally larger than 90% (Table 3). The measured spectra of all samples were normalized to equal neutron flux by means of a $^{6}$Li–glass monitor located close to the neutron target. The transmission spectra measured with a second $^{6}$Li glass detector at a flight path of 260 cm were used for a rough determination of the total cross sections. Though the accuracy of this method is inferior to that obtained in a dedicated experiment, these total cross sections can be used for testing the normalization to equal neutron flux (Sec. 3).

## 2.3 Measurements

The samples were moved cyclically into the measuring position by a computer controlled sample changer. The data acquisition time per sample was about 10–15 min, a complete cycle lasting about 2 h. From each event, a 64 bit word was recorded on DAT tape containing the sum energy and TOF information together with 42 bits identifying those

Table 2: ISOTOPIC COMPOSITIONS (%)

| Sample | Isotope | | | | | | | Analysis |
|---|---|---|---|---|---|---|---|---|
| | $^{142}$Nd | $^{143}$Nd | $^{144}$Nd | $^{145}$Nd | $^{146}$Nd | $^{148}$Nd | $^{150}$Nd | |
| $^{142}$Nd | 95.0 | 2.7 | 1.5 | 0.3 | 0.3 | 0.1 | 0.1 | IPPE, original values |
| | 95.51 | 2.44 | 1.46 | 0.23 | 0.27 | 0.06 | 0.03 | IPPE, final analysis |
| | 95.73 | 2.43 | 1.25 | 0.22 | 0.27 | 0.06 | 0.04 | FZK |
| $^{143}$Nd | 13.5 | 53.2 | 30.5 | 1.3 | 1.3 | 0.1 | 0.1 | IPPE, original values |
| | 13.40 | 53.47 | 30.53 | 1.15 | 1.29 | 0.11 | 0.05 | IPPE, final analysis |
| $^{144}$Nd | 2.7 | 5.7 | 81.5 | 7.9 | 2.0 | 0.2 | 0.0 | IPPE, original values |
| | 2.58 | 5.51 | 82.07 | 7.78 | 1.89 | 0.11 | 0.06 | IPPE, final analysis |
| | 2.61 | 5.51 | 82.13 | 7.83 | 1.75 | 0.11 | 0.06 | FZK |
| $^{145}$Nd | 1.0 | 0.9 | 7.9 | 70.8 | 18.8 | 0.4 | 0.2 | IPPE, original values |
| | 0.98 | 0.83 | 8.02 | 71.15 | 18.54 | 0.32 | 0.16 | IPPE, final analysis |
| $^{146}$Nd | 0.6 | 1.1 | 1.6 | 2.9 | 91.4 | 2.2 | 0.2 | IPPE, original values |
| | 0.71 | 0.55 | 1.90 | 2.57 | 91.77 | 2.26 | 0.24 | IPPE, final analysis |
| $^{148}$Nd | 1.3 | 1.0 | 2.8 | 4.1 | 9.8 | 78.3 | 2.7 | IPPE, original values |
| | 1.29 | 1.01 | 2.75 | 4.19 | 9.92 | 78.16 | 2.68 | IPPE, final analysis |

Table 3: CALCULATED NEUTRON TRANSMISSION[1]

| Sample | Neutron Energy (keV) | | | | |
|---|---|---|---|---|---|
| | 10 | 20 | 40 | 80 | 160 |
| $^{197}$Au | 0.972 | 0.976 | 0.980 | 0.983 | 0.986 |
| $^{142}$Nd | 0.916 | 0.921 | 0.926 | 0.932 | 0.937 |
| $^{143}$Nd | 0.936 | 0.947 | 0.955 | 0.961 | 0.966 |
| $^{144}$Nd | 0.857 | 0.873 | 0.890 | 0.905 | 0.919 |
| $^{145}$Nd | 0.964 | 0.970 | 0.975 | 0.979 | 0.981 |
| $^{146}$Nd | 0.916 | 0.925 | 0.933 | 0.941 | 0.948 |
| $^{148}$Nd | 0.900 | 0.915 | 0.930 | 0.942 | 0.953 |

[1] Monte Carlo calculation with the SESH code [26].

Table 4: PARAMETERS OF THE INDIVIDUAL RUNS

| Run | Flight Path (mm) | TOF Scale (ns/ch) | Number of Cycles | Maximum Neutron Energy (keV) | Measuring Time (d) | Average Beam Current ($\mu$A) | Threshold in Sum Energy (MeV) |
|---|---|---|---|---|---|---|---|
| I | 786.6 | 0.7603 | 187 | 200 | 15.7 | 1.6 | 1.6 |
| II | 786.6 | 0.7603 | 280 | 100 | 21.9 | 1.7 | 1.4 |
| III | 786.8 | 0.7103 | 212 | 100 ADC | 17.0 | 1.6 | 1.4 |
| IV | 786.7 | 0.7095 | 184 | 100 ADC | 18.3 | 1.3 | 1.7 |

detector modules that contributed. In total, 4 different runs were carried out using neutron spectra with different maximum energies. The relevant parameters are listed in Table 4. The data in Runs III and IV were recorded with the ADC system. In the first analysis of Run III a systematic difference in the cross section ratios was found with respect to the results of Runs I and II. When this run was repeated with a slightly modified time adjustment in the ADC system, it was recognized that the discrepancy was due to a problem in the detector electronics which could be removed by a modification in the sorting procedure (see Sec.3). Therefore, both runs with the ADC system could be included in the final analysis. The overall recorded information was 52 Gbyte. In the first two runs $^{208}$Pb was used as the scattering sample while graphite was used in Runs III and IV.

# 3 DATA ANALYSIS

## 3.1 Total Cross Sections

The total cross sections of the neodymium isotopes were determined in the neutron energy range from 10 to 200 keV via the TOF spectra measured with the $^{6}$Li glass detector at a flight path of 260 cm. The total cross sections and the related uncertainties were obtained as described in Ref.[22], and are listed in Table 5. The values deduced for the carbon sample agree with the data from the Joint Evaluated File (JEF) [27] within $\pm$3.4%, similar to the measurements reported in Refs.[22, 28]. These results confirm the accuracy obtained in normalizing the spectra of the individual samples to equal neutron flux, since the above results can only be obtained if the uncertainty of this correction is smaller than 0.2%. The combined results of the four runs agree with the JEF data in the energy range from 15 to 100 keV to better than 1%. The quoted uncertainties were obtained under the assumption that they are inversely proportional to the fraction of neutrons interacting in the sample, A=1–T, where T is the transmission. For the carbon sample this fraction is A=5.5%, and a related uncertainty of 3.4% was estimated from the comparison with the JEF data.

The oxygen cross section was adopted from the JEF evaluation and its uncertainty was neglected. Hence, the uncertainty of the measured cross section was entirely ascribed to the respective neodymium isotope. For the samples with low enrichment, the uncertainty was attributed to the main isotope after correction for isotopic impurities.

The total cross section determined for the $^{208}$Pb sample is in good agreement with the data of Ref.[29]. The total cross section of elemental neodymium was calculated with the assumption that the cross sections for $^{148}$Nd and $^{150}$Nd are equal. These data agree within 2% with the results of Seth *et al.* [30] between 10 and 200 keV, except for a step-like structure in the cross section which appears at 20 keV in Ref.[30] but was found at 40 keV in the present experiment. This step is mainly due to the strong scattering resonances between 30 and 40 keV in the abundant $^{142}$Nd [31].

Table 5: MEASURED TOTAL CROSS SECTIONS [1]

| Neutron Energy (keV) | Total Cross Section (barn) | | | | | | | | |
|---|---|---|---|---|---|---|---|---|---|
| | $^{142}$Nd | $^{143}$Nd | $^{144}$Nd | $^{145}$Nd | $^{146}$Nd | $^{148}$Nd | $^{208}$Pb | $^{12}$C | $^{197}$Au |
| 10 – 15 | 7.8 | 14.3 | 13.7 | 17.5 | 12.7 | 17.3 | 11.0 | 4.82 | 15.4 |
| 15 – 20 | 7.9 | 13.6 | 12.8 | 12.7 | 13.0 | 21.9 | 10.8 | 4.49 | 14.0 |
| 20 – 30 | 6.1 | 14.1 | 16.4 | 12.3 | 12.9 | 17.5 | 11.1 | 4.91 | 14.5 |
| 30 – 40 | 13.6 | 11.2 | 12.3 | 11.5 | 10.6 | 17.2 | 11.3 | 4.94 | 13.3 |
| 40 – 60 | 7.1 | 8.9 | 11.3 | 8.9 | 10.1 | 21.7 | 10.5 | 4.94 | 11.1 |
| 60 – 80 | 6.1 | 8.4 | 10.1 | 8.4 | 11.3 | 13.9 | 14.6 | 4.56 | 11.1 |
| 80 – 100 | 6.8 | 9.4 | 8.7 | 8.4 | 9.7 | 13.2 | 10.8 | 4.54 | 11.7 |
| 100 – 150 | 6.0 | 9.0 | 8.3 | 8.6 | 9.2 | 10.0 | 10.8 | | 13.3 |
| 150 – 200 | 6.2 | 6.0 | 6.7 | 5.3 | 7.5 | 8.4 | 9.0 | | 8.2 |
| Uncertainty | 3.4% | 5.4% | 2.1% | 8.5% | 3.4% | 3.0% | 2.9% | 3.4% | 9.4% |

[1] determined from the count rate of the $^{6}$Li glass neutron monitor at 260 cm flight path

It has to be mentioned, that a systematic effect in the evaluation of the total cross sections had been overlooked in the previous measurements on rare earth isotopes with the $4\pi BaF_2$ detector, where the nominal sample thickness of 22 mm was adopted in data analysis. While this is correct for the determination of the capture cross sections, where the diameter of the neutron beam is larger that of the sample, the situation is different in the transmission geometry with the neutron beam being smaller than the sample diameter. In this case, the true diameter has to be taken into account by considering the volume changes during the sintering process. This caused an average reduction of the sample diameter by 4% in the present experiment, while the gadolinium samples in Ref. [20] shrinked by only 1% on average. For the ealier study on samarium isotopes, however, this effect could not be recovered [22]. The present total cross sections could be determined with uncertainties between ~2% and ~10% for sample transmissions between 0.90% and 0.98%, respectively.

## 3.2 Capture Cross Sections

The analysis was carried out in the same way as described previously [21, 22, 24]. All events were sorted into two–dimensional spectra containing 128 sum energy versus 2048 TOF channels according to various event multiplicities (Evaluation 1). In Evaluation 2, this procedure was repeated by rejecting those events, where only neighboring detector modules contributed to the sum energy signal. With this option, background from the natural radioactivity of the $BaF_2$ crystals and from scattered neutrons can be reduced. For all samples, the resulting spectra were normalized to equal neutron flux using the count rate of the $^{6}$Li glass monitor close to the neutron target. The corresponding normalization

Table 6: MATRIX FOR ISOTOPIC CORRECTIONS[1] (%)

| Corrected spectrum | Measured spectrum | | | | | | Corrected sample thickness ($10^{-3}$ at/barn) |
|---|---|---|---|---|---|---|---|
| | $^{142}$Nd | $^{143}$Nd | $^{144}$Nd | $^{145}$Nd | $^{146}$Nd | $^{148}$Nd | |
| $^{142}$Nd | 100 | –10.146 | –0.054 | –1.008 | –0.291 | –0.116 | 6.2985 |
| $^{143}$Nd | –5.849 | 100 | –15.786 | +4.937 | –0.715 | –0.046 | 1.5216 |
| $^{144}$Nd | –1.243 | –23.757 | 100 | –43.211 | +0.332 | –0.170 | 5.4776 |
| $^{145}$Nd | –0.133 | –0.194 | –1.998 | 100 | –6.508 | +0.079 | 1.0694 |
| $^{146}$Nd | –0.375 | –1.167 | –1.094 | –10.080 | 100 | –3.757 | 4.3152 |
| $^{148}$Nd | –0.511 | –1.718 | –1.015 | –12.109 | –11.464 | 100 | 2.8213 |

[1]The abundance of $^{150}$Nd has been multiplied by a factor of 1.82 and added to the abundance of $^{146}$Nd (see text).

factors are below 0.5% for all runs. The treatment of the two–dimensional spectra from the data recorded with the ADC system is slightly more complicated and was performed as described in Ref. [22].

Due to an accidental offset in the calibration of the linear gates analyzing the energy signals of the individual detectors, $\gamma$–rays below 80 keV were suppressed while the corresponding time signals were still processed. This mismatch caused only a small deterioration in the energy resolution of the sum–energy signals in the calorimeter mode, but had severe consequences for the data taken with the ADC system. In this mode, events were only accepted by the data analysis code if both signals, from the time and energy channels, were provided. Therefore, more of the soft $\gamma$–ray cascades from captures in the gold sample were rejected than neodymium capture events, resulting in a systematic difference of $\sim$ 10% in the cross section ratios obtained with the ADC system and with the calorimeter mode. This discrepancy was disappeared after the sorting procedure was modified accordingly (see Sec.4).

In the next step of data analysis, sample–independent backgrounds were removed by subtracting the spectra measured with the empty sample canning. A remaining constant background was determined at very long flight times, where no time–correlated events are expected. The resulting two–dimensional spectra for events with multiplicity >2 measured in Run II are shown for all investigated neodymium samples in Figs. 2, 3, and 4.

At this point, the spectra contain only events that are correlated with the sample. The next correction to be made is for isotopic impurities (see Ref.[22] for details). The respective coefficients are compiled in Table 6. Captures in $^{150}$Nd, the only isotope not measured in the present experiment, were approximated by the spectrum of $^{146}$Nd, which has a very similar binding energy. The $^{150}$Nd abundance was scaled by a factor of 1.82 according to the cross section ratio [4].

The $^{143}$Nd and $^{144}$Nd samples required rather large corrections for isotopic impurities.

Fig. 5 shows the projection of the two–dimensional spectra of $^{143}$Nd and $^{144}$Nd on the sum energy axis before and after this correction. The indicated structures are caused by the isotopic impurities of $^{144}$Nd and $^{145}$Nd, respectively. However, most of this background is due to sample scattered neutrons which are captured in the Ba isotopes of the scintillator. This component is removed by subtracting the background spectrum measured with the $^{208}$Pb scattering sample (after normalization in a region above the binding energy of the investigated isotope, i.e. above channels 101 and 77 for $^{143}$Nd and $^{144}$Nd, respectively). The final spectra (right side of Fig.5) compare well with the respective spectra of the $^{145}$Nd and $^{148}$Nd samples, where both corrections are significantly smaller.

In Fig. 6, the TOF spectra before subtraction of the background from isotopic impurities are shown together with this background. In the $^{143}$Nd and $^{144}$Nd spectra, about 25% of the observed effect is due to isotopic impurities, whereas the 10% for $^{142}$Nd are typical for all other isotopes, which are not shown explicitely.

For the determination of the $^{142}$Nd cross section, the spectroscopic features of the $4\pi BaF_2$ detector becomes particularly important. Due to the neutron shell closure at N=82, the cross sections of the neighboring isotopes are up to eight times bigger. Thus, even the small $^{143}$Nd impurity of 2.7% causes a significant correction. In experiments using the pulse height weighting technique this effect is even enhanced since the detector efficiency is proportional to the neutron separation energy, requiring an impurity correction of $\sim$30%. With the $4\pi BaF_2$ detector this correction is three times smaller, since the contribution from $^{143}$Nd is concentrated at higher sum energies, and can be discriminated in the evaluation of the $^{142}$Nd cross section.

As already discussed in Ref. [20] the present correction for isotopic impurities holds exactly only if all samples are about equal in weight: only then second order effects due to neutron multiple scattering and self–shielding are properly accounted for. In the present experiment the largest correction occurs for the $^{144}$Nd sample due to the $^{145}$Nd admixture of 7.8%. The weight of the two samples differs by a factor of 4.6. Therefore, calculating the correction directly from the isotope matrix leads to an overcompensation due to the smaller self–shielding in the thin $^{145}$Nd sample. Thanks to the good energy resolution of the $4\pi BaF_2$ detector, this effect can be verified experimentally in the corrected sum–energy spectrum of $^{144}$Nd as a negative peak located at the binding energy of $^{145}$Nd. Removing this overcompensation by a 12.5% reduction of the respective correction factor in the isotope matrix resulted in a 2% increase in the $^{144}$Nd cross section. For all other isotopes such an overcompensation was not observed.

Following the correction for isotopic impurities, the background due to capture of sample scattered neutrons was removed from the spectra by means of the data measured with the scattering samples. This correction, which is sizable since the neodymium isotopes exhibit fairly large total-to-capture cross section ratios, was determined as described previously [22]. The correction is facilitated due to the low binding energies involved. As shown in Fig. 5, even for the odd isotope $^{143}$Nd with the largest binding energy, the respective capture events are sufficiently separated from the peaks due to captures of scattered neutrons in the odd barium isotopes, so that this background can be reliably normalized.

The corrections for capture of scattered neutrons are included in Fig. 7, and their influence at different neutron energies is given in Table 7 for the runs with maximum

neutron energies of 100 keV and 200 keV. Comparison with the respective spectra from the barium experiment [19] shows that the signal to background ratio is significantly better in the present case though the cross section of $^{142}$Nd is almost two times smaller than those of $^{136}$Ba and $^{137}$Ba. This reduction of background from scattered neutrons results from the use of oxide samples instead of the carbonate, that had to be accepted for the barium samples. Furthermore, the binding energy of $^{142}$Nd is only 6.1 MeV and, therefore, the capture events are more easily separated from the background peaks due to capture of scattered neutrons in the even barium isotopes (see Fig.5).

After this last correction, the final spectra contain only the net capture events of the investigated isotopes (bottom spectra in Figs. 2, 3, and 4).

For the first time, two different scattering samples (graphite and $^{208}$Pb) have been used in the same experiment. Therefore, the respective differences are discussed in some detail. The low mass number of graphite implies that the scattered neutrons are slightly less energetic compared to neutrons scattered from the capture samples investigated with the $4\pi BaF_2$ detector ($93<A<181$). This energy difference results in a small delay in TOF and, hence, may affect the scattering correction as illustrated in Fig.8, where the TOF spectra of the scattering samples are compared with a cut from the $^{148}$Nd spectrum containing only scattered neutrons. The binding energy of $^{148}$Nd being only 5.0 MeV allowed to separate the pure scattering component by setting a lower threshold of 5.6 MeV in the $\gamma$-spectrum (corresponding to channel 67 in Fig.9).

Table 7: SIGNAL/BACKGROUND RATIO FOR RUNS WITH DIFFERENT MAXIMUM NEUTRON ENERGY

| Sample | $\sigma_t/\sigma_\gamma$[1] | Maximum neutron energy | Signal/Background ratio[2] | | |
|---|---|---|---|---|---|
| | $E_n$=30 keV | (keV) | $E_n$=30 keV | 20 keV | 10 keV |
| $^{142}$Nd | 500 | 100 | 1.7 | 1.1 | 1.2 |
| $^{143}$Nd | 80 | | 3.2 | 1.9 | 1.3 |
| $^{144}$Nd | 280 | | 2.2 | 1.5 | 1.3 |
| $^{145}$Nd | 40 | | 4.9 | 2.6 | 1.7 |
| $^{146}$Nd | 200 | | 3.0 | 1.8 | 1.3 |
| $^{148}$Nd | 180 | | 4.1 | 2.2 | 1.5 |
| $^{197}$Au | 24 | | 10.2 | 4.1 | 2.8 |
| | | | | | |
| $^{142}$Nd | | 200 | 1.5 | 1.1 | 1.1 |
| $^{143}$Nd | | | 2.9 | 1.8 | 1.3 |
| $^{144}$Nd | | | 1.9 | 1.4 | 1.1 |
| $^{145}$Nd | | | 4.5 | 2.5 | 1.8 |
| $^{146}$Nd | | | 2.5 | 1.7 | 1.2 |
| $^{148}$Nd | | | 3.4 | 2.0 | 1.5 |
| $^{197}$Au | | | 8.1 | 3.6 | 2.6 |

[1]Total cross section including oxygen

[2]defined as (effect+neutron scattering background)/(neutron scattering background)

Figure 2: The different steps of background subtraction illustrated for $^{142}$Nd and $^{145}$Nd. The two–dimensional sum energy $\times$ TOF spectra represent events with multiplicity $>2$ and were measured in Run II with 100 keV maximum neutron energy. (The original resolution of 128 $\times$ 2048 channels was compressed into 64 $\times$ 64 channels for better readability. The correction for isotopic impurities is omitted since the difference is hardly visible in these spectra).

Figure 3: Same as Fig. 2 but for the $^{143}$Nd and $^{144}$Nd samples.

Figure 4: Same as Fig. 2 but for the $^{146}$Nd and $^{148}$Nd samples.

Figure 5: Sum energy spectra of the $^{143}$Nd and $^{144}$Nd samples before and after the corrections for isotopic impurities and background due to scattered neutrons. The middle panel shows the respective spectrum for the scattering sample.

Figure 6: TOF spectra of the $^{142}$Nd, $^{143}$Nd, and $^{144}$Nd samples. The background due to isotopic impurities is shown separately.

The spectra due to neutrons scattered from the $^{148}$Nd sample and the scattering samples are quite similar, but the respective ratios, which are plotted with reduced resolution in the lower part, exhibit significant differences. For the carbon sample, this scattering correction shows a pronounced peak in the TOF interval between channels 1425 and 1475 as a result of the larger energy loss in the scattering process; correspondingly, no such peak occurs for the $^{208}$Pb sample.

The influence of this effect on the evaluated capture cross sections is much less spectacular, however, since it occurs in a TOF range just at the onset of the scattering correction where the absolute count rate are small. Therefore, the delay of scattering events related to the carbon sample is in reality a tiny effect, which needs to be considered only, because it is located in the TOF interval used for the absolute normalization of the measured cross sections.

The slight decrease of the scattering correction with neutron energy follows from the energy dependence of the respective total cross sections which are given in Table 5. The cross sections of $^{208}$Pb and carbon are almost constant whereas the $^{148}$Nd cross section is significantly decreasing with neutron energy. This dependence is somewhat more pronounced for $^{208}$Pb than for the graphite sample, the relative differences between maximum and minimum corrections being 1.3 and 1.2, respectively.

As demonstrated in Fig. 8, the scattering correction exhibits strong variations with TOF. It is, therefore, an important advantage that the good energy resolution of the $4\pi$BaF$_2$ detector allows to determine the scattering correction as a function of neutron energy. This feature is missing in experiments based on detection techniques with no or poor resolution in $\gamma$-energy, which have to assume a constant normalization factor, an approximation that may be responsible for significant systematic uncertainties.

Two further remarks have to be added with respect to Fig. 8. The scattering corrections of Fig. 7 show a small but significant step in the high energy edge of the $^{208}$Pb spectrum due to the strong resonance at 78.2 keV. This weak structure has little influence on the further analysis. In addition, all scattering corrections exhibit a broad peak around channel 1180 corresponding to a neutron energy of 21 keV which is most obvious in the background spectrum of the $^{142}$Nd sample. This feature is caused by capture events in the strong $^{19}$F resonance at 27.1 keV which has a peak cross section of 2 barn. Hence, scattered neutrons with the proper energy are captured in the very first cm of the scintillator, but the additional TOF due to 10 cm distance between sample and the detector modules shifts these events to 21 keV on the energy scale of the primary beam.

The $^{142}$Nd spectrum of Fig. 7 shows resolved resonances up to 20 keV neutron energy. Therefore, individual resonance parameters will also be extracted by a shape analysis code as for $^{136}$Ba [32] and for some tin isotopes [33], but similar to those cases, significant differences for the final stellar cross sections are not to be expected.

After subtraction of the scattering background, the TOF spectra of Fig. 7 were used to determine the cross section shape. For normalization, the two–dimensional data were projected onto the sum energy axis using the TOF region of optimum signal to background ratio as indicated in Fig. 7 by dashed boxes. The resulting pulse height spectra are shown in Fig. 9 for the events with multiplicity >2. Note, that the threshold in sum energy could be lowered to 1.4 MeV. Two features in the spectra have to be discussed. In case of $^{142}$Nd, there is a small bump around channel 105, corresponding to captures in

Figure 7: TOF spectra of the neodymium samples measured in Run II (100 keV maximum neutron energy, $^{208}$Pb scattering sample). The background due to sample scattered neutrons is shown separately. The region used for the absolute normalization of the cross section is indicated by hatched boxes.

Figure 8: The correction for capture of scattered neutrons for $^{148}$Nd from the comparison with the spectra obtained with a $^{208}$Pb and a graphite sample.

the odd Ba isotopes of the scintillator which reflects the statistical uncertainties in the normalization of the scattering correction. By comparison with the spectrum of the $^{208}$Pb sample in Fig. 5 the related uncertainty for the capture events in $^{142}$Nd is found to be very small and is, therefore, included in the counting statistics. In the spectrum of the $^{144}$Nd sample there is a small bipolar structure around channel 90. This is an artefact from the correction of isotopic impurities due to capture in $^{143}$Nd, probably caused by a small shift in energy of the respective capture events in the $^{142}$Nd and the $^{143}$Nd sample. This feature is considered by a corresponding uncertainty assumed for this correction (see Section 5).

In Fig.10, the sum energy spectra of the neodymium isotopes are shown for different multiplicities. These multiplicities correspond to the number of detector modules contributing per event. The true multiplicities are slightly smaller, because of cross talking effects. In the even isotopes, 30 to 40% of the capture events are observed with multiplicities $\geq$5, while the respective fraction in the odd isotopes is about 80%, rather large values in view of the proximity of the closed neutron shell N=82. The arrows in Fig. 10 indicate the range of sum energy channels that were integrated to obtain the TOF spectra of Fig. 7, from which the cross section shapes were determined.

The cross section ratio of isotope X relative to the gold standard is given by

$$\frac{\sigma_i(X)}{\sigma_i(Au)} = \frac{Z_i(X)}{Z_i(Au)} \cdot \frac{\Sigma Z(Au)}{\Sigma Z(X)} \cdot \frac{\Sigma E(X)}{\Sigma E(Au)} \cdot \frac{m(Au)}{m(X)} \cdot F_1 \cdot F_2. \qquad (1)$$

Figure 9: Sum energy spectra of all isotopes measured in Run II containing events with multiplicity >2. These spectra were obtained by projection of the two–dimensional spectra in the TOF region below the maximum neutron energy as indicated by hatched boxes in Fig. 7.

In this expression, $Z_i$ is the count rate in channel $i$ of the TOF spectrum, $\Sigma Z$ is the TOF rate integrated over the interval used for normalization (Fig.7), $\Sigma E$ is the total count rate in the sum energy spectrum for all multiplicities summed over the normalization interval (Fig.10), and m is the sample thickness in atoms/barn. The factor $F_1$ = (100–f(Au))/(100–f(X)) corrects for the fraction of capture events f below the experimental threshold in sum energy, where X refers to the respective neodymium sample (Table 9), and $F_2$ is the ratio of the multiple scattering and self–shielding corrections .

The values ΣE in eq.1 were not simply determined by adding the individual countrates of multiplicity one to five, but in a slightly modified way, which is described in detail by means of Fig.11. It is obvious from Fig. 10 that the ΣE–entries are mainly determined by the count rates for multiplicity >2 while the statistical uncertainties are dominated by the few events with multiplicity one. For the Nd isotopes, multiplicity one contributes less than 4% of the total intensity but 85% to the statistical uncertainty. In order to reduce this disproportion, the interval B between the threshold and pulse height channel 50 for multiplicity one was eliminated from the analysis and the respective intensity was determined by extrapolation. For all investigated isotopes, the ratios of the total intensities (A+B) and of part A are plotted for multiplicities two to five (open circles in Fig.11). These data can be extrapolated by a smooth curve to multiplicity one (open square), thus determining the part B for multiplicity one with an assumed uncertainty of 5%. The figure shows that the extrapolated values are inversely proportional to the binding energies, which are linearly decreasing from $^{142}$Nd to $^{148}$Nd. This behaviour is expected if the shape of the sum–energy spectra is equal for all isotopes. Compared to the straightforward analysis, the actual values of ΣE are modified by less than 0.7%, but the uncertainties are reduced by 25 to 30%.

A second detail of the evaluation, which has not been documented so far, refers to Eq. 1 being valid only for Evaluation 1. In Evaluation 2, where part of the events are rejected to reduce backgrounds, true capture events may also be lost. The true intensity is, therefore, calculated via

$$\Sigma E(X)_{true} = \Sigma E(X)_{eval2} \cdot \frac{\Sigma A(X)_{eval1}}{\Sigma A(X)_{eval2}} \tag{2}$$

where ΣA(X) is the intensity of part A in Fig.11 summed over all multiplicities. Thus a third correction factor is introduced into equation 1,

$$F_3 = \frac{\Sigma A(X)_{eval1}}{\Sigma A(X)_{eval2}} \cdot \frac{\Sigma A(Au)_{eval2}}{\Sigma A(Au)_{eval1}} \tag{3}$$

The respective values are compiled for all runs in Table 8. The fraction of lost events is between 8 and 12% for the even neodymium isotopes and for the gold sample. In these cases, the effect tends to cancel out in the ratio, leading to small corrections $F_3$. For the odd isotopes, however, the larger multiplicities result in losses of only 1 – 2%, giving rise to correspondingly larger corrections.

The fraction of unobserved capture events, f, and the correction factor $F_1$ were calculated as described in detail in Ref.[24]. The required input for this calculation are the individual neutron capture cascades and their relative contributions to the total capture cross section as well as the detector efficiency for monoenergetic $\gamma$–rays in the energy range up to 10 MeV. Capture cascades and capture $\gamma$–ray spectra of the involved isotopes were calculated according to the statistical and optical models [34] as in the previous measurements with the $4\pi$ $BaF_2$ detector [19, 21, 22]. The calculations are based on the Hauser-Feshbach approach. In Table 10, the calculated cross sections are given as a function of cascade multiplicity together with the $\gamma$–ray energies of the 20 most probable cascades. The respective capture $\gamma$–ray spectra are shown in Fig. 12.

Table 8: CORRECTION FACTOR $F_3$ FOR EVALUATION 2

| Cross section ratio | Run I | Run II | Run III | Run IV |
|---|---|---|---|---|
| $^{142}$Nd/Au | 1.0357 | 1.0106 | 1.0093 | 0.9954 |
| $^{143}$Nd/Au | 0.9356 | 0.9289 | 0.9249 | 0.9343 |
| $^{144}$Nd/Au | 1.0496 | 1.0394 | 1.0381 | 1.0344 |
| $^{145}$Nd/Au | 0.9302 | 0.9268 | 0.9267 | 0.9307 |
| $^{146}$Nd/Au | 1.0250 | 1.0134 | 1.0105 | 1.0194 |
| $^{148}$Nd/Au | 0.9957 | 0.9853 | 0.9893 | 0.9891 |

The efficiency of the $4\pi$ $BaF_2$ detector was determined experimentally [35] by measuring the response for monoenergetic $\gamma$–rays, which were produced by (p,$\gamma$)–reactions on thin $^{26}$Mg, $^{30}$Si, and $^{34}$S targets. In these reactions, certain proton resonances decay predominantly by two-step cascades. Replacing one of the $BaF_2$ modules by a Ge–detector and looking for $BaF_2$–Ge–coincidences, two–dimensional spectra, $E_\gamma$(Ge) versus $E_\gamma$($BaF_2$), were recorded. The response of the $4\pi$ $BaF_2$ detector for monoenergetic $\gamma$–rays was then obtained by selecting those events, where the full energy of the complementary $\gamma$–ray is registered in the Ge–detector.

Using seven (p,$\gamma$)–resonances and an $^{88}$Y source, the line shapes of 20 $\gamma$–transitions in the energy range from 0.843 to 8.392 MeV could be determined. These data were used in the calculation of the spectrum fractions, f, and of the correction factors, $F_1$, given in Table 9. The resulting sum–energy spectra shown in Fig. 13 are in good agreement with the experimental spectra of Fig. 9, thus confirming the calculation of the correction factors $F_1$. Due to the low threshold energy of 1.4 MeV, the detection efficiency exceeds 97% for all isotopes despite of the low binding energies of the even Nd isotopes.

As in case of the samarium isotopes [22], the average multiplicities of the neodymium capture cascades are between 3.2 and 4.5, and a significant part of the cross section refers to cascades with multiplicities 6 and 7, resulting in long computing times for the determination of the theoretical sum energy spectra. Nevertheless, these calculations were repeated five times for each isotope starting from different sets of random numbers to simulate the finite solid angle, a necessary precaution that was noticed previously [19]. Since even with a modern workstation several months were required for these calculations, it was attempted to solve this problem via the Monte Carlo technique by randomly selecting the pulse height of an individual $\gamma$–ray in the capture cascade from the measured probability distribution for monoenergetic $\gamma$–rays. The comparison of both calculations in Table 9 yields typical differences of only 0.3% for threshold energies of 1.4 and 1.6 MeV. For the present evaluation, the results of the exact calculation were used.

As in all previous experiments with the $4\pi$ $BaF_2$ detector, the correction factor $F_1$ was found to depend linearly on the binding energy of the captured neutron (Fig.14).

Table 9: FRACTION OF UNDETECTED CAPTURE EVENTS, f (%), AND THE RELATED CORRECTION FACTORS $F_1$. [1]

| | Threshold in sum energy (MeV) | | | | | | |
|---|---|---|---|---|---|---|---|
| | 1.0 | 1.4 | 1.5 | 1.6 | 1.7 | 2.0 | |
| f(Au) | 2.18 | | 3.30 | | | 4.93 | |
| f($^{142}$Nd) | 1.09 | | 1.99 | | | 3.90 | |
| f($^{143}$Nd) | 0.45 | | 1.06 | | | 1.64 | Exact |
| f($^{144}$Nd) | 1.84 | | 3.39 | | | 5.39 | calculation |
| f($^{145}$Nd) | 0.38 | | 0.91 | | | 1.50 | |
| f($^{146}$Nd) | 1.98 | | 3.72 | | | 5.97 | |
| f($^{148}$Nd) | 1.84 | | 3.94 | | | 6.53 | |
| $F_1$($^{142}$Nd/Au) | 0.989 | 0.987 | 0.987 | 0.987 | 0.988 | 0.989 | |
| $F_1$($^{143}$Nd/Au) | 0.983 | 0.978 | 0.977 | 0.976 | 0.973 | 0.967 | |
| $F_1$($^{144}$Nd/Au) | 0.997 | 1.000 | 1.001 | 1.002 | 1.003 | 1.005 | |
| $F_1$($^{145}$Nd/Au) | 0.982 | 0.977 | 0.976 | 0.974 | 0.972 | 0.965 | |
| $F_1$($^{146}$Nd/Au) | 0.998 | 1.003 | 1.004 | 1.005 | 1.007 | 1.011 | |
| $F_1$($^{148}$Nd/Au) | 0.997 | 1.005 | 1.007 | 1.009 | 1.011 | 1.017 | |
| f(Au) | 2.32 | | 3.42 | | | 4.95 | |
| f($^{142}$Nd) | 1.44 | | 2.54 | | | 5.04 | |
| f($^{143}$Nd) | 0.42 | | 0.96 | | | 1.53 | Monte Carlo |
| f($^{144}$Nd) | 2.30 | | 4.24 | | | 5.89 | calculation |
| f($^{145}$Nd) | 0.49 | | 1.17 | | | 1.65 | |
| f($^{146}$Nd) | 2.03 | | 3.99 | | | 6.37 | |
| f($^{148}$Nd) | 1.94 | | 4.25 | | | 6.75 | |
| $F_1$($^{142}$Nd/Au) | 0.991 | 0.991 | 0.991 | 0.993 | 0.995 | 1.001 | |
| $F_1$($^{143}$Nd/Au) | 0.981 | 0.976 | 0.975 | 0.973 | 0.971 | 0.965 | |
| $F_1$($^{144}$Nd/Au) | 1.000 | 1.007 | 1.009 | 1.009 | 1.009 | 1.010 | |
| $F_1$($^{145}$Nd/Au) | 0.982 | 0.978 | 0.977 | 0.975 | 0.973 | 0.966 | |
| $F_1$($^{146}$Nd/Au) | 0.997 | 1.004 | 1.006 | 1.008 | 1.010 | 1.015 | |
| $F_1$($^{148}$Nd/Au) | 0.996 | 1.006 | 1.009 | 1.011 | 1.013 | 1.019 | |

[1] Solid angle 96%, $\gamma$–ray threshold 50 keV

Figure 10: Sum energy spectra of all neodymium isotopes as a function of multiplicity. The regions used to determine the cross section shape are indicated by arrows.

Table 10: CALCULATED CAPTURE GAMMA–RAY CASCADES INCLUDING MULTIPLICITIES, PARTIAL CROSS SECTIONS, $\sigma_p$, AND GAMMA–RAY ENERGIES OF THE 20 MOST SIGNIFICANT CASCADES

$^{142}$Nd

| | |
|---|---|
| $\sigma$(30 keV)=30.5 mb | total capture cross section [1] |
| $\sigma$(mul 1)=0.5 mb | |
| $\sigma$(mul 2)=5.9 mb | |
| $\sigma$(mul 3)=12.3 mb | |
| $\sigma$(mul 4)=9.3 mb | average multiplicity <m>=3.2 |
| $\sigma$(mul 5)=2.3 mb | |
| $\sigma$(mul 6)=0.2 mb | |

447 cascades covering 95% of the cross section

| $\sigma_p$ (mb) | $\sigma_p/\sigma$ (%) | $E_{\gamma 1}$ | $E_{\gamma 2}$ | $E_{\gamma 3}$ | $E_{\gamma 4}$ |
|---|---|---|---|---|---|
| | | | (MeV) | | |
| 1.37 | 4.5 | 5.410 | 0.742 | | |
| 1.05 | 3.4 | 3.656 | 1.754 | 0.742 | |
| 0.91 | 3.0 | 3.656 | 2.496 | | |
| 0.88 | 2.9 | 4.646 | 0.764 | 0.742 | |
| 0.84 | 2.8 | 4.596 | 0.814 | 0.742 | |
| 0.81 | 2.6 | 4.544 | 0.866 | 0.742 | |
| 0.81 | 2.6 | 3.250 | 2.161 | 0.742 | |
| 0.72 | 2.4 | 3.250 | 2.902 | | |
| 0.66 | 2.2 | 4.846 | 0.564 | 0.742 | |
| 0.63 | 2.1 | 2.844 | 2.567 | 0.742 | |
| 0.62 | 2.0 | 4.377 | 1.033 | 0.742 | |
| 0.56 | 1.8 | 2.844 | 3.308 | | |
| 0.50 | 1.6 | 4.353 | 1.057 | 0.742 | |
| 0.49 | 1.6 | 2.437 | 2.973 | 0.742 | |
| 0.47 | 1.5 | 6.152 | | | |
| 0.42 | 1.4 | 2.437 | 3.715 | | |
| 0.35 | 1.2 | 2.031 | 3.379 | 0.742 | |
| 0.32 | 1.0 | 4.156 | 1.996 | | |
| 0.29 | 0.96 | 2.844 | 1.753 | 0.814 | 0.742 |
| 0.29 | 0.95 | 3.250 | 1.346 | 0.814 | 0.742 |
| | $\Sigma$=42.5% | | | | |

[1] normalized to present experimental value

TABLE 10 (continued)

$^{143}$Nd

| | |
|---|---|
| $\sigma$(100 keV)=235.0 mb | total capture cross section [1] |
| $\sigma$(mul 1)=0.1 mb | |
| $\sigma$(mul 2)=5.2 mb | |
| $\sigma$(mul 3)=34.0 mb | |
| $\sigma$(mul 4)=78.5 mb | average multiplicity <m>=4.5 |
| $\sigma$(mul 5)=73.3 mb | |
| $\sigma$(mul 6)=34.0 mb | |
| $\sigma$(mul 7)=9.9 mb | |

841 cascades covering 95% of the cross section

| $\sigma_p$ (mb) | $\sigma_p/\sigma$ (%) | $E_{\gamma 1}$ | $E_{\gamma 2}$ | $E_{\gamma 3}$ (MeV) | $E_{\gamma 4}$ | $E_{\gamma 5}$ |
|---|---|---|---|---|---|---|
| 4.65 | 2.0 | 3.869 | 2.663 | 0.618 | 0.697 | |
| 4.46 | 1.9 | 4.422 | 2.110 | 0.618 | 0.697 | |
| 4.30 | 1.8 | 3.316 | 3.216 | 0.618 | 0.697 | |
| 3.68 | 1.6 | 4.975 | 2.176 | 0.697 | | |
| 3.62 | 1.5 | 4.422 | 2.728 | 0.697 | | |
| 3.56 | 1.5 | 4.975 | 1.558 | 0.618 | 0.697 | |
| 3.55 | 1.5 | 6.532 | 0.618 | 0.697 | | |
| 3.55 | 1.5 | 2.764 | 3.769 | 0.618 | 0.697 | |
| 3.36 | 1.4 | 3.869 | 3.281 | 0.697 | | |
| 3.19 | 1.4 | 3.869 | 2.467 | 0.814 | 0.697 | |
| 2.97 | 1.3 | 3.316 | 3.834 | 0.697 | | |
| 2.97 | 1.3 | 4.422 | 1.914 | 0.814 | 0.697 | |
| 2.96 | 1.3 | 3.316 | 3.020 | 0.814 | 0.697 | |
| 2.86 | 1.2 | 7.150 | 0.697 | | | |
| 2.54 | 1.1 | 2.211 | 4.321 | 0.618 | 0.697 | |
| 2.49 | 1.1 | 6.336 | 0.814 | 0.697 | | |
| 2.45 | 1.0 | 2.764 | 4.387 | 0.697 | | |
| 2.42 | 1.0 | 2.764 | 3.573 | 0.814 | 0.697 | |
| 2.21 | 0.94 | 2.764 | 2.211 | 1.558 | 0.618 | 0.697 |
| 2.17 | 0.92 | 4.975 | 1.362 | 0.814 | 0.697 | |
| | $\Sigma$=27.3% | | | | | |

[1] normalized to present experimental value

TABLE 10 (continued)

$^{144}$Nd

| | |
|---|---|
| $\sigma$(30 keV)=72. mb | total capture cross section [1] |
| $\sigma$(mul 1)=0.4 mb | |
| $\sigma$(mul 2)=9.4 mb | |
| $\sigma$(mul 3)=31.4 mb | average multiplicity <m>=3.4 |
| $\sigma$(mul 4)=24.4 mb | |
| $\sigma$(mul 5)=5.7 mb | |
| $\sigma$(mul 6)=0.7 mb | |

823 cascades covering 95% of the cross section

| $\sigma_p$ (mb) | $\sigma_p/\sigma$ (%) | $E_{\gamma 1}$ | $E_{\gamma 2}$ | $E_{\gamma 3}$ | $E_{\gamma 4}$ |
|---|---|---|---|---|---|
| | | | (MeV) | | |
| 2.79 | 3.9 | 5.718 | 0.067 | | |
| 2.60 | 3.6 | 3.789 | 1.929 | 0.067 | |
| 2.05 | 2.8 | 3.368 | 2.350 | 0.067 | |
| 1.76 | 2.4 | 3.789 | 1.924 | 0.072 | |
| 1.60 | 2.2 | 2.947 | 2.771 | 0.067 | |
| 1.45 | 2.0 | 3.368 | 2.345 | 0.072 | |
| 1.22 | 1.7 | 2.526 | 3.192 | 0.067 | |
| 1.17 | 1.6 | 4.459 | 1.259 | 0.067 | |
| 1.16 | 1.6 | 2.947 | 2.766 | 0.072 | |
| 1.14 | 1.6 | 5.713 | 0.072 | | |
| 1.05 | 1.5 | 4.865 | 0.853 | 0.067 | |
| 0.97 | 1.4 | 4.252 | 1.461 | 0.072 | |
| 0.96 | 1.3 | 4.700 | 1.018 | 0.067 | |
| 0.89 | 1.2 | 2.526 | 3.187 | 0.072 | |
| 0.88 | 1.2 | 2.105 | 3.613 | 0.067 | |
| 0.79 | 1.1 | 4.571 | 1.147 | 0.067 | |
| 0.78 | 1.1 | 3.789 | 1.996 | | |
| 0.76 | 1.1 | 4.384 | 1.401 | | |
| 0.67 | 0.93 | 3.368 | 2.417 | | |
| 0.65 | 0.90 | 2.105 | 3.608 | 0.072 | |
| | $\Sigma$=35.1% | | | | |

[1] normalized to experimental value

TABLE 10 (continued)

$^{145}$Nd

| | |
|---|---|
| $\sigma$(100 keV)=410.0 mb | total capture cross section [1] |
| $\sigma$(mul 1)=0.1 mb | |
| $\sigma$(mul 2)=8.0 mb | |
| $\sigma$(mul 3)=61.5 mb | |
| $\sigma$(mul 4)=138.0 mb | average multiplicity <m>=4.5 |
| $\sigma$(mul 5)=128.0 mb | |
| $\sigma$(mul 6)=58.6 mb | |
| $\sigma$(mul 7)=15.8 mb | |

588 cascades covering 95% of the cross section

| $\sigma_p$ (mb) | $\sigma_p/\sigma$ (%) | $E_{\gamma 1}$ | $E_{\gamma 2}$ | $E_{\gamma 3}$ (MeV) | $E_{\gamma 4}$ | $E_{\gamma 5}$ |
|---|---|---|---|---|---|---|
| 9.03 | 2.2 | 4.126 | 2.425 | 0.589 | 0.454 | |
| 8.85 | 2.2 | 3.537 | 3.015 | 0.589 | 0.454 | |
| 7.41 | 1.8 | 4.715 | 1.836 | 0.589 | 0.454 | |
| 7.36 | 1.8 | 2.947 | 3.604 | 0.589 | 0.454 | |
| 6.23 | 1.5 | 4.715 | 2.425 | 0.454 | | |
| 6.07 | 1.5 | 4.126 | 3.014 | 0.454 | | |
| 5.83 | 1.4 | 5.305 | 1.835 | 0.454 | | |
| 5.58 | 1.4 | 3.537 | 3.604 | 0.454 | | |
| 5.32 | 1.3 | 6.551 | 0.589 | 0.454 | | |
| 5.23 | 1.3 | 2.358 | 4.194 | 0.589 | 0.454 | |
| 5.00 | 1.2 | 4.126 | 2.278 | 0.736 | 0.454 | |
| 4.90 | 1.2 | 3.537 | 2.868 | 0.736 | 0.454 | |
| 4.70 | 1.1 | 2.947 | 4.193 | 0.454 | | |
| 4.33 | 1.1 | 2.358 | 2.358 | 1.836 | 0.589 | 0.454 |
| 4.25 | 1.0 | 4.715 | 1.689 | 0.736 | 0.454 | |
| 4.25 | 1.0 | 2.947 | 2.358 | 1.835 | 0.454 | |
| 4.20 | 1.0 | 2.947 | 1.768 | 1.836 | 0.589 | 0.454 |
| 4.18 | 1.0 | 2.947 | 3.457 | 0.736 | 0.454 | |
| 4.13 | 1.0 | 7.140 | 0.454 | | | |
| 4.12 | 1.0 | 3.537 | 2.540 | 0.475 | 0.589 | 0.454 |
| | $\Sigma$=27.0% | | | | | |

[1] normalized to present experimental value

TABLE 10 (continued)

$^{146}$Nd

| | |
|---|---|
| $\sigma$(30 keV)=89.0 mb | total capture cross section [1] |
| $\sigma$(mul 1)=0.7 mb | |
| $\sigma$(mul 2)=10.3 mb | |
| $\sigma$(mul 3)=23.0 mb | average multiplicity <m>=4.0 |
| $\sigma$(mul 4)=24.8 mb | |
| $\sigma$(mul 5)=18.8 mb | |
| $\sigma$(mul 6)=9.0 mb | |
| $\sigma$(mul 7)=2.4 mb | |

1000 cascades covering 93% of the cross section

| $\sigma_p$ (mb) | $\sigma_p/\sigma$ (%) | $E_{\gamma 1}$ | $E_{\gamma 2}$ | $E_{\gamma 3}$ (MeV) | $E_{\gamma 4}$ | $E_{\gamma 5}$ |
|---|---|---|---|---|---|---|
| 2.46 | 2.8 | 4.201 | 1.122 | | | |
| 1.52 | 1.7 | 3.734 | 1.588 | | | |
| 1.30 | 1.5 | 2.800 | 1.400 | 1.122 | | |
| 1.20 | 1.3 | 2.334 | 1.867 | 1.122 | | |
| 1.19 | 1.3 | 3.267 | 0.933 | 1.122 | | |
| 1.17 | 1.3 | 5.007 | 0.315 | | | |
| 1.11 | 1.2 | 3.267 | 2.055 | | | |
| 1.08 | 1.2 | 4.201 | 0.807 | 0.315 | | |
| 1.07 | 1.2 | 4.201 | 0.994 | 0.078 | 0.050 | |
| 0.97 | 1.1 | 4.201 | 0.907 | 0.087 | 0.078 | 0.050 |
| 0.93 | 1.0 | 1.867 | 2.334 | 1.122 | | |
| 0.86 | 0.97 | 3.734 | 0.467 | 1.122 | | |
| 0.85 | 0.96 | 3.734 | 1.273 | 0.315 | | |
| 0.85 | 0.96 | 2.800 | 2.522 | | | |
| 0.77 | 0.87 | 5.107 | 0.087 | 0.078 | 0.050 | |
| 0.77 | 0.87 | 3.734 | 1.460 | 0.078 | 0.050 | |
| 0.73 | 0.82 | 3.267 | 1.740 | 0.315 | | |
| 0.70 | 0.79 | 4.201 | 1.072 | 0.050 | | |
| 0.64 | 0.72 | 5.322 | | | | |
| 0.64 | 0.72 | 2.334 | 2.989 | | | |
| | $\Sigma$=23.3% | | | | | |

[1] normalized to experimental value

TABLE 10 (continued)

$^{148}$Nd

| | |
|---|---|
| $\sigma$(100 keV)=132.0 mb | total capture cross section [1] |
| $\sigma$(mul 1)=0.2 mb | |
| $\sigma$(mul 2)=8.6 mb | |
| $\sigma$(mul 3)=36.0 mb | |
| $\sigma$(mul 4)=49.3 mb | average multiplicity <m>=4.0 |
| $\sigma$(mul 5)=28.3 mb | |
| $\sigma$(mul 6)=8.2 mb | |
| $\sigma$(mul 7)=1.4 mb | |

2737 cascades covering 95% of the cross section

| $\sigma_p$ (mb) | $\sigma_p/\sigma$ (%) | $E_{\gamma 1}$ | $E_{\gamma 2}$ | $E_{\gamma 3}$ (MeV) | $E_{\gamma 4}$ |
|---|---|---|---|---|---|
| 2.09 | 1.6 | 4.030 | 1.038 | | |
| 1.64 | 1.2 | 4.030 | 0.873 | 0.165 | |
| 1.25 | 0.95 | 4.030 | 0.705 | 0.333 | |
| 1.17 | 0.89 | 4.030 | 0.900 | 0.138 | |
| 1.11 | 0.84 | 2.687 | 1.343 | 1.038 | |
| 1.06 | 0.80 | 3.135 | 0.896 | 1.038 | |
| 1.03 | 0.78 | 4.030 | 0.780 | 0.258 | |
| 0.99 | 0.75 | 2.239 | 1.791 | 1.038 | |
| 0.98 | 0.74 | 3.583 | 1.485 | | |
| 0.85 | 0.64 | 3.583 | 1.321 | 0.165 | |
| 0.84 | 0.64 | 3.583 | 0.448 | 1.038 | |
| 0.80 | 0.61 | 4.030 | 0.753 | 0.120 | 0.165 |
| 0.80 | 0.61 | 2.687 | 1.343 | 0.705 | 0.333 |
| 0.80 | 0.61 | 3.135 | 0.896 | 0.705 | 0.333 |
| 0.78 | 0.59 | 3.583 | 1.152 | 0.333 | |
| 0.75 | 0.57 | 1.791 | 2.239 | 1.038 | |
| 0.70 | 0.53 | 4.903 | 0.165 | | |
| 0.69 | 0.52 | 2.239 | 1.791 | 0.705 | 0.333 |
| 0.67 | 0.51 | 4.030 | 0.563 | 0.475 | |
| 0.66 | 0.51 | 3.583 | 0.448 | 0.705 | 0.333 |
| | $\Sigma$=14.9% | | | | |

[1] normalized to present experimental value

Figure 11: Extrapolation of the contributions from capture events with low energy and multiplicity 1 (see text).

The correction for neutron multiple scattering and self–shielding was calculated with the SESH code [26]. Apart from the pairing energies [36], most of the input parameters were adopted from Ref.[31]. These parameters were slightly modified in order to reproduce the measured total and capture cross sections. The final values are listed in Table 11 together with the calculated total cross sections. The resulting correction factors, MS(X) and $F_2$, are compiled in Tables 12 and 13.

Since the enrichment of some samples is comparably low, these corrections were calculated either for the true sample composition or for that part which remains after the correction for isotopic impurities. Most samples of the present experiment being very similar in weight and size allowed to assume that subtraction of the isotopic impurities via the spectra of the other samples accounts for the respective contributions to the multiple scattering corrections as well. Therefore, the cross sections were determined using the corrections obtained by assuming that the samples consisted of the main isotopes only. In general, these corrections are small, e.g. below 2%, but can be sizable for the even isotopes at energies below 10 keV (see also Sec.5).

Figure 12: Calculated capture $\gamma$–ray spectra for the neodymium isotopes.

Figure 13: Calculated sum energy spectra of the $4\pi BaF_2$ detector based on the measured lineshapes. These spectra were used to derive the correction $F_1$ for unobserved capture events.

Figure 14: The correction $F_1$ for unobserved capture events, plotted versus the difference in binding energy between the investigated neodymium isotopes and the gold standard for two different sum energy thresholds.

Table 11: PARAMETERS FOR THE CALCULATION OF NEUTRON SELF–SHIELDING AND MULTIPLE SCATTERING CORRECTIONS

| Parameter | | $^{142}$Nd | $^{143}$Nd | $^{144}$Nd | $^{145}$Nd | $^{146}$Nd | $^{148}$Nd | $^{16}$O |
|---|---|---|---|---|---|---|---|---|
| Nucleon Number | | 142 | 143 | 144 | 145 | 146 | 148 | 16 |
| Binding Energy (MeV) | | 6.123 | 7.817 | 5.756 | 7.565 | 5.292 | 5.039 | 4.144 |
| Pairing Energy (MeV) | | 1.18 | 1.94 | 1.18 | 2.10 | 1.18 | 1.18 | 0.0 |
| Effective Temperature (K) | | 293 | 293 | 293 | 293 | 293 | 293 | 293 |
| Nuclear Spin | | 0 | 3.5 | 0 | 3.5 | 0 | 0 | 0 |
| Average Radiation | s | 0.030 | 0.120 | 0.070 | 0.090 | 0.040 | 0.070 | 0.0 |
| Width (eV) | p | 0.044 | 0.031 | 0.070 | 0.060 | 0.050 | 0.040 | 0.0 |
| Average Level | s | 500. | 40. | 370. | 20. | 200. | 120. | 0.0 |
| Spacing (eV) | p[1] | 167. | 20. | 123. | 10. | 66.7 | 40. | 0.0 |
| Strength Function | $S_0$ | 1.5 | 3.2 | 4.0 | 3.7 | 2.6 | 5.0 | 0.0 |
| ($10^{-4}$) | $S_1$ | 0.4 | 0.8 | 0.5 | 0.8 | 0.5 | 0.3 | 0.0 |
| Nuclear Radius | s | 5.6 | 5.25 | 6.0 | 5.25 | 7.2 | 8.0 | 5.5 |
| (fm) | p | 5.6 | 5.25 | 6.0 | 5.25 | 7.2 | 8.0 | 0.0 |
| | | Calculated total cross sections | | | | | | |
| 3 keV | | 15.3 | 27.6 | 34.6 | 31.4 | 26.0 | 45.2 | 3.80 |
| 5 keV | | 12.7 | 22.2 | 27.7 | 25.1 | 21.5 | 36.5 | 3.80 |
| 10 keV | | 10.1 | 16.6 | 20.7 | 18.6 | 16.9 | 27.5 | 3.79 |
| 20 keV | | 8.22 | 12.7 | 15.6 | 14.1 | 13.5 | 20.9 | 3.77 |
| 40 keV | | 6.86 | 9.83 | 11.9 | 10.8 | 11.0 | 15.9 | 3.74 |
| 80 keV | | 5.84 | 7.74 | 9.09 | 8.33 | 8.95 | 11.8 | 3.68 |
| 160 keV | | 5.09 | 6.18 | 6.87 | 6.51 | 7.22 | 8.22 | 3.55 |
| 320 keV | | 4.58 | 5.04 | 5.15 | 5.16 | 5.73 | 5.28 | 3.31 |

[1]Calculated with SESH [26]

Table 12: CORRECTION FACTORS FOR NEUTRON SELF–SHIELDING AND MULTIPLE SCATTERING, MS

| Energy Bin | MS | | | | | | |
|---|---|---|---|---|---|---|---|
| (keV) | $^{197}$Au | $^{142}$Nd | $^{143}$Nd | $^{144}$Nd | $^{145}$Nd | $^{146}$Nd | $^{148}$Nd |
| 3 – 5 | 1.005 | 0.825 | 0.977 | 0.790 | 1.001 | 0.852 | 0.869 |
| 5 – 7.5 | 1.018 | 0.908 | 0.999 | 0.880 | 1.011 | 0.928 | 0.933 |
| 7.5 – 10 | 1.025 | 0.943 | 1.007 | 0.935 | 1.015 | 0.971 | 0.970 |
| 10 – 12.5 | 1.029 | 0.963 | 1.010 | 0.971 | 1.017 | 0.997 | 0.992 |
| 12.5 –15 | 1.030 | 0.973 | 1.012 | 0.985 | 1.018 | 1.006 | 1.002 |
| 15 – 20 | 1.031 | 0.984 | 1.014 | 1.002 | 1.018 | 1.014 | 1.011 |
| 20 – 25 | 1.032 | 0.994 | 1.015 | 1.011 | 1.017 | 1.018 | 1.017 |
| 25 – 30 | 1.032 | 1.001 | 1.016 | 1.016 | 1.017 | 1.020 | 1.021 |

TABLE 12 (continued)

| | | | | | | | |
|---|---|---|---|---|---|---|---|
| 30 – 40 | 1.031 | 1.008 | 1.017 | 1.021 | 1.017 | 1.021 | 1.024 |
| 40 – 50 | 1.030 | 1.012 | 1.017 | 1.025 | 1.016 | 1.023 | 1.026 |
| 50 – 60 | 1.029 | 1.015 | 1.017 | 1.026 | 1.016 | 1.024 | 1.027 |
| 60 – 80 | 1.028 | 1.018 | 1.016 | 1.027 | 1.015 | 1.024 | 1.027 |
| 80 – 100 | 1.027 | 1.019 | 1.015 | 1.027 | 1.015 | 1.025 | 1.027 |
| 100 – 120 | 1.026 | 1.020 | 1.015 | 1.028 | 1.014 | 1.025 | 1.027 |
| 120 – 150 | 1.024 | 1.021 | 1.014 | 1.028 | 1.013 | 1.025 | 1.026 |
| 150 – 175 | 1.023 | 1.021 | 1.014 | 1.028 | 1.013 | 1.025 | 1.025 |
| 175 – 200 | 1.022 | 1.021 | 1.013 | 1.027 | 1.012 | 1.025 | 1.024 |
| 200 – 225 | 1.021 | 1.021 | 1.013 | 1.027 | 1.012 | 1.025 | 1.023 |
| Uncertainty (%) | 0.3 | 0.7 | 0.6 | 0.8 | 0.3 | 0.5 | 0.8 |

Table 13: CORRECTION FACTORS FOR THE CROSS SECTION RATIOS, $F_2$ = MS(Au)/MS(X)

| Energy Bin | $F_2$ | | | | | |
|---|---|---|---|---|---|---|
| (keV) | $^{142}$Nd/Au | $^{143}$Nd/Au | $^{144}$Nd/Au | $^{145}$Nd/Au | $^{146}$Nd/Au | $^{148}$Nd/Au |
| 3 – 5 | 1.218 | 1.029 | 1.272 | 1.004 | 1.180 | 1.157 |
| 5 – 7.5 | 1.121 | 1.019 | 1.157 | 1.007 | 1.097 | 1.091 |
| 7.5– 10 | 1.087 | 1.018 | 1.096 | 1.010 | 1.056 | 1.057 |
| 10 – 12.5 | 1.069 | 1.019 | 1.060 | 1.012 | 1.032 | 1.037 |
| 12.5 – 15 | 1.059 | 1.018 | 1.046 | 1.012 | 1.024 | 1.028 |
| 15 – 20 | 1.048 | 1.017 | 1.029 | 1.013 | 1.017 | 1.020 |
| 20 – 25 | 1.038 | 1.017 | 1.021 | 1.015 | 1.014 | 1.015 |
| 25 – 30 | 1.031 | 1.016 | 1.016 | 1.015 | 1.012 | 1.011 |
| 30 – 40 | 1.023 | 1.014 | 1.010 | 1.014 | 1.010 | 1.007 |
| 40 – 50 | 1.018 | 1.013 | 1.005 | 1.014 | 1.007 | 1.004 |
| 50 – 60 | 1.014 | 1.012 | 1.003 | 1.013 | 1.005 | 1.002 |
| 60 – 80 | 1.010 | 1.012 | 1.001 | 1.013 | 1.004 | 1.001 |
| 80 – 100 | 1.008 | 1.012 | 1.000 | 1.012 | 1.002 | 1.000 |
| 100 – 120 | 1.006 | 1.011 | 0.998 | 1.012 | 1.001 | 0.999 |
| 120 – 150 | 1.003 | 1.010 | 0.996 | 1.011 | 0.999 | 0.998 |
| 150 – 175 | 1.002 | 1.009 | 0.995 | 1.010 | 0.998 | 0.998 |
| 175 – 200 | 1.001 | 1.009 | 0.995 | 1.010 | 0.997 | 0.998 |
| 200 – 225 | 1.000 | 1.008 | 0.994 | 1.009 | 0.996 | 0.998 |
| Uncertainty (%) | 0.8 | 0.7 | 0.9 | 0.4 | 0.6 | 0.8 |

# 4 RESULTS FOR THE NEUTRON CAPTURE CROSS SECTIONS

The measured neutron capture cross section ratios of the neodymium isotopes and of $^{197}$Au are listed in Tables 14 to 19 together with the respective statistical uncertainties. The data are given for all runs and for the two evaluations discussed in Sec.3 separately. The last column in each table contains the weighted average, the weight being determined by the inverse of the squared statistical uncertainties. Since the cross section ratios depend weakly on energy, the averages for the energy interval from 30 to 80 keV are also included to allow for a better comparison of the individual results. The data are free of systematic differences with respect to the different runs or evaluations. This is particularly important for the comparison of Runs I and II with III and IV which were performed with different data acquisition modes and different scattering samples. For example, the results from Evaluation 2 – for the average of all samples – exceed those of Evaluation 1 by only 0.7%. The results of Runs I and II, which were measured in the calorimeter mode, are on average lower by 0.5% compared to the mean, while the data measured with the ADC system in Runs III and IV are higher by 0.8%. The largest discrepancy is found for the results of Run IV, which are higher by 1.5% compared to the mean. All these differences, however, are well compatible with the respective statistical uncertainties. Even the 1.5% difference observed in Run IV represents only two standard deviations of the statistical uncertainty introduced by the gold sample in the absolute normalization of the cross section.

As in the previous measurements with the $4\pi$ $BaF_2$ detector [19, 21, 22], the final cross section ratios were adopted from Evaluation 2. The respective mean values are compiled for all runs in Table 20 together with the statistical, systematic, and total uncertainties. The energy bins are sufficiently fine to avoid systematic uncertainties in the calculation of the Maxwellian averaged cross sections (Sec.6). The final uncertainties of the cross section ratios are less than 2.5% for all isotopes in the energy range from 30 to 100 keV but exceed 10% at the lowest energy bin in case of the even isotopes. For $^{142}$Nd, the lowest data point in the energy bin from 3 to 5 keV carries an uncertainty of >30% and was, therefore, not considered in the evaluation of the stellar cross sections (see Sec.6).

The experimental ratios were converted into absolute cross sections using the gold cross section of Macklin [37] after normalization by a factor of 0.989 to the value of Ratynski and Käppeler [38] (Table 21). The uncertainties of these data can be obtained by adding the 1.5% uncertainty of the reference cross section to the uncertainties of the respective cross section ratios.

The present results are compared with the data of Mathews and Käppeler [9] in Figures 15 to 17. Though uncertainties of 5 to 10% are quoted for these data, the present results for the even isotopes $^{142}$Nd and $^{144}$Nd are systematically lower by ∼30%, while good agreement is only found for the $^{143}$Nd cross section. A general comparison with all other data will be discussed in Sec.6 in connection with the stellar cross sections.

Table 14: $\sigma(^{142}\mathrm{Nd})/\sigma(^{197}\mathrm{Au})$ AND STATISTICAL UNCERTAINTIES IN (%)

| Energy Bin (keV) | Run I | | Run II | | Run III | | Run IV | | Average | |
|---|---|---|---|---|---|---|---|---|---|---|
| Evaluation 1 | | | | | | | | | | |
| 3 – 5 | – | – | 0.0196 | 94.1 | 0.0375 | 66.7 | – | – | 0.0315 | 54.4 |
| 5 – 7.5 | 0.0704 | 23.6 | 0.0342 | 31.1 | 0.0609 | 22.2 | 0.0180 | 98.7 | 0.0579 | 14.6 |
| 7.5 – 10 | 0.0677 | 19.7 | 0.0395 | 22.4 | 0.0666 | 17.5 | 0.0752 | 19.9 | 0.0638 | 10.0 |
| 10 – 12.5 | 0.0235 | 40.9 | 0.0195 | 33.2 | 0.0300 | 27.7 | 0.0324 | 31.7 | 0.0271 | 16.5 |
| 12.5 – 15 | 0.0473 | 19.7 | 0.0533 | 10.6 | 0.0661 | 11.4 | 0.0684 | 13.6 | 0.0600 | 6.4 |
| 15 – 20 | 0.0347 | 15.2 | 0.0276 | 12.0 | 0.0644 | 7.2 | 0.0587 | 9.5 | 0.0537 | 5.1 |
| 20 – 25 | 0.0719 | 6.0 | 0.0655 | 4.2 | 0.0714 | 5.6 | 0.0605 | 7.7 | 0.0676 | 2.7 |
| 25 – 30 | 0.0503 | 5.9 | 0.0457 | 4.1 | 0.0391 | 6.9 | 0.0362 | 8.9 | 0.0446 | 2.9 |
| 30 – 40 | 0.0619 | 3.4 | 0.0557 | 2.4 | 0.0643 | 3.5 | 0.0628 | 4.2 | 0.0598 | 1.6 |
| 40 – 50 | 0.0678 | 3.1 | 0.0605 | 2.2 | 0.0624 | 3.5 | 0.0634 | 4.1 | 0.0629 | 1.5 |
| 50 – 60 | 0.0673 | 3.1 | 0.0650 | 1.9 | 0.0649 | 3.2 | 0.0681 | 3.8 | 0.0658 | 1.4 |
| 60 – 80 | 0.0663 | 2.6 | 0.0676 | 1.6 | 0.0666 | 2.8 | 0.0690 | 3.4 | 0.0673 | 1.2 |
| 80 – 100 | 0.0670 | 2.5 | 0.0620 | 1.7 | 0.0645 | 2.9 | 0.0645 | 3.4 | 0.0639 | 1.2 |
| 100 – 120 | 0.0663 | 2.5 | 0.0636 | 1.8 | 0.0658 | 3.1 | 0.0653 | 3.8 | 0.0648 | 1.3 |
| 120 – 150 | 0.0692 | 2.3 | – | – | – | – | – | – | 0.0692 | 2.3 |
| 150 – 175 | 0.0627 | 2.4 | – | – | – | – | – | – | 0.0627 | 2.4 |
| 175 – 200 | 0.0671 | 2.4 | – | – | – | – | – | – | 0.0671 | 2.4 |
| 200 – 225 | 0.0652 | 3.4 | – | – | – | – | – | – | 0.0652 | 3.4 |
| 30 – 80 | 0.0658 | 2.2 | 0.0622 | 1.7 | 0.0646 | 2.9 | 0.0658 | 3.4 | 0.0640 | 1.1 |
| Evaluation 2 | | | | | | | | | | |
| 3 – 5 | – | – | 0.0369 | 38.1 | 0.0202 | 89.9 | 0.0242 | 88.9 | 0.0330 | 33.3 |
| 5 – 7.5 | 0.0619 | 20.0 | 0.0556 | 14.3 | 0.0480 | 20.3 | 0.0385 | 32.6 | 0.0538 | 9.7 |
| 7.5 – 10 | 0.0545 | 18.3 | 0.0591 | 11.6 | 0.0728 | 11.5 | 0.0731 | 13.9 | 0.0661 | 6.6 |
| 10 – 12.5 | 0.0281 | 25.5 | 0.0437 | 11.4 | 0.0353 | 17.2 | 0.0377 | 19.2 | 0.0392 | 8.1 |
| 12.5 – 15 | 0.0613 | 11.3 | 0.0660 | 6.6 | 0.0776 | 7.4 | 0.0757 | 9.0 | 0.0708 | 4.1 |
| 15 – 20 | 0.0427 | 9.4 | 0.0389 | 6.7 | 0.0495 | 6.7 | 0.0567 | 7.0 | 0.0474 | 3.7 |
| 20 – 25 | 0.0726 | 4.6 | 0.0678 | 3.3 | 0.0714 | 4.1 | 0.0667 | 5.1 | 0.0695 | 2.1 |
| 25 – 30 | 0.0545 | 4.2 | 0.0525 | 3.0 | 0.0446 | 4.6 | 0.0415 | 5.7 | 0.0500 | 2.0 |
| 30 – 40 | 0.0636 | 2.6 | 0.0608 | 1.9 | 0.0651 | 2.5 | 0.0645 | 2.9 | 0.0631 | 1.2 |
| 40 – 50 | 0.0641 | 2.5 | 0.0631 | 1.9 | 0.0634 | 2.5 | 0.0629 | 2.9 | 0.0633 | 1.2 |
| 50 – 60 | 0.0640 | 2.5 | 0.0655 | 1.7 | 0.0646 | 2.3 | 0.0666 | 2.7 | 0.0652 | 1.1 |
| 60 – 80 | 0.0656 | 2.0 | 0.0673 | 1.5 | 0.0650 | 2.0 | 0.0668 | 2.4 | 0.0663 | 0.9 |
| 80 –100 | 0.0654 | 2.0 | 0.0628 | 1.5 | 0.0624 | 2.0 | 0.0629 | 2.4 | 0.0634 | 1.0 |
| 100 –120 | 0.0639 | 2.0 | 0.0624 | 1.7 | 0.0625 | 2.2 | 0.0632 | 2.7 | 0.0629 | 1.0 |
| 120 –150 | 0.0669 | 1.8 | – | – | – | – | – | – | 0.0669 | 1.8 |
| 150 –175 | 0.0618 | 1.9 | – | – | – | – | – | – | 0.0618 | 1.9 |
| 175 –200 | 0.0650 | 1.9 | – | – | – | – | – | – | 0.0650 | 1.9 |
| 200 –225 | 0.0612 | 2.8 | – | – | – | – | – | – | 0.0621 | 2.8 |
| 30 – 80 | 0.0643 | 1.7 | 0.0642 | 1.5 | 0.0645 | 2.0 | 0.0652 | 2.4 | 0.0645 | 0.9 |

Table 15: $\sigma(^{143}\mathrm{Nd})/\sigma(^{197}\mathrm{Au})$ AND STATISTICAL UNCERTAINTIES IN (%)

| Energy Bin (keV) | Run I | | Run II | | Run III | | Run IV | | Average | |
|---|---|---|---|---|---|---|---|---|---|---|
| Evaluation 1 | | | | | | | | | | |
| 3 – 5 | 0.4132 | 15.2 | 0.4156 | 10.9 | 0.5324 | 9.8 | 0.4140 | 12.6 | 0.4562 | 5.9 |
| 5 – 7.5 | 0.3559 | 11.3 | 0.4041 | 7.0 | 0.4757 | 6.3 | 0.4200 | 8.1 | 0.4287 | 3.8 |
| 7.5 – 10 | 0.4301 | 8.0 | 0.4221 | 5.8 | 0.4633 | 5.7 | 0.4453 | 6.8 | 0.4415 | 3.2 |
| 10 – 12.5 | 0.3662 | 6.8 | 0.3950 | 4.7 | 0.3992 | 4.8 | 0.4095 | 5.2 | 0.3957 | 2.6 |
| 12.5 – 15 | 0.4420 | 5.7 | 0.4301 | 3.8 | 0.4461 | 3.9 | 0.4764 | 4.2 | 0.4484 | 2.1 |
| 15 – 20 | 0.4209 | 3.5 | 0.4340 | 2.4 | 0.4317 | 2.5 | 0.4265 | 2.8 | 0.4296 | 1.3 |
| 20 – 25 | 0.4508 | 2.7 | 0.4650 | 1.8 | 0.4568 | 2.1 | 0.4606 | 2.3 | 0.4595 | 1.1 |
| 25 – 30 | 0.4474 | 2.1 | 0.4426 | 1.5 | 0.4544 | 1.7 | 0.4518 | 1.9 | 0.4487 | 0.9 |
| 30 – 40 | 0.4235 | 1.6 | 0.4101 | 1.2 | 0.4165 | 1.2 | 0.4246 | 1.3 | 0.4177 | 0.7 |
| 40 – 50 | 0.4214 | 1.6 | 0.4128 | 1.2 | 0.4171 | 1.2 | 0.4278 | 1.4 | 0.4190 | 0.7 |
| 50 – 60 | 0.4057 | 1.6 | 0.3957 | 1.2 | 0.4098 | 1.2 | 0.4163 | 1.3 | 0.4062 | 0.6 |
| 60 – 80 | 0.4076 | 1.3 | 0.4030 | 1.0 | 0.3978 | 1.0 | 0.4090 | 1.1 | 0.4036 | 0.5 |
| 80 – 100 | 0.3866 | 1.3 | 0.3872 | 1.0 | 0.3854 | 1.0 | 0.4017 | 1.1 | 0.3899 | 0.5 |
| 100 – 120 | 0.3774 | 1.3 | 0.3789 | 1.1 | 0.3838 | 1.1 | 0.3915 | 1.3 | 0.3826 | 0.6 |
| 120 – 150 | 0.3628 | 1.2 | – | – | – | – | – | – | 0.3628 | 1.2 |
| 150 – 175 | 0.3518 | 1.3 | – | – | – | – | – | – | 0.3518 | 1.3 |
| 175 – 200 | 0.3491 | 1.3 | – | – | – | – | – | – | 0.3491 | 1.3 |
| 200 – 225 | 0.3422 | 1.9 | – | – | – | – | – | – | 0.3422 | 1.9 |
| 30 – 80 | 0.4146 | 1.2 | 0.4054 | 1.1 | 0.4103 | 1.1 | 0.4194 | 1.3 | 0.4116 | 0.6 |
| Evaluation 2 | | | | | | | | | | |
| 3 – 5 | 0.4564 | 11.1 | 0.4383 | 7.7 | 0.4735 | 8.0 | 0.4151 | 9.7 | 0.4470 | 4.4 |
| 5 – 7.5 | 0.3774 | 8.2 | 0.4205 | 4.9 | 0.4713 | 4.7 | 0.4331 | 6.1 | 0.4358 | 2.8 |
| 7.5 – 10 | 0.4341 | 6.1 | 0.4524 | 4.2 | 0.4414 | 4.5 | 0.4404 | 5.1 | 0.4437 | 2.4 |
| 10 – 12.5 | 0.3897 | 5.0 | 0.4039 | 3.5 | 0.3907 | 3.7 | 0.4247 | 4.0 | 0.4031 | 2.0 |
| 12.5 – 15 | 0.4657 | 4.1 | 0.4340 | 2.9 | 0.4526 | 3.1 | 0.4774 | 3.4 | 0.4545 | 1.7 |
| 15 – 20 | 0.4198 | 2.7 | 0.4419 | 1.8 | 0.4344 | 2.0 | 0.4347 | 2.3 | 0.4348 | 1.1 |
| 20 – 25 | 0.4669 | 2.1 | 0.4721 | 1.5 | 0.4620 | 1.6 | 0.4704 | 1.9 | 0.4680 | 0.9 |
| 25 – 30 | 0.4458 | 1.7 | 0.4458 | 1.2 | 0.4547 | 1.3 | 0.4525 | 1.6 | 0.4497 | 0.7 |
| 30 – 40 | 0.4258 | 1.2 | 0.4169 | 1.0 | 0.4219 | 1.0 | 0.4280 | 1.3 | 0.4222 | 0.5 |
| 40 – 50 | 0.4205 | 1.3 | 0.4179 | 1.0 | 0.4194 | 1.0 | 0.4261 | 1.3 | 0.4204 | 0.6 |
| 50 – 60 | 0.4022 | 1.3 | 0.3983 | 1.0 | 0.4093 | 1.0 | 0.4165 | 1.3 | 0.4059 | 0.6 |
| 60 – 80 | 0.4072 | 1.0 | 0.4010 | 0.8 | 0.4007 | 0.8 | 0.4085 | 1.1 | 0.4033 | 0.4 |
| 80 –100 | 0.3857 | 1.0 | 0.3870 | 0.8 | 0.3860 | 0.8 | 0.3987 | 1.1 | 0.3884 | 0.5 |
| 100 –120 | 0.3759 | 1.1 | 0.3758 | 0.9 | 0.3841 | 0.9 | 0.3854 | 1.3 | 0.3800 | 0.5 |
| 120 –150 | 0.3606 | 1.0 | – | – | – | – | – | – | 0.3606 | 1.0 |
| 150 –175 | 0.3462 | 1.1 | – | – | – | – | – | – | 0.3462 | 1.1 |
| 175 –200 | 0.3443 | 1.1 | – | – | – | – | – | – | 0.3443 | 1.1 |
| 200 –225 | 0.3353 | 1.6 | – | – | – | – | – | – | 0.3353 | 1.6 |
| 30 – 80 | 0.4139 | 0.9 | 0.4085 | 0.9 | 0.4128 | 0.8 | 0.4198 | 1.1 | 0.4130 | 0.5 |

Table 16: $\sigma(^{144}\mathrm{Nd})/\sigma(^{197}\mathrm{Au})$ AND STATISTICAL UNCERTAINTIES IN (%)

| Energy Bin (keV) | Run I | | Run II | | Run III | | Run IV | | Average | |
|---|---|---|---|---|---|---|---|---|---|---|
| Evaluation 1 | | | | | | | | | | |
| 3 – 5 | 0.0925 | 46.3 | 0.1030 | 28.4 | 0.1039 | 35.8 | 0.0794 | 50.4 | 0.0983 | 18.7 |
| 5 – 7.5 | 0.1122 | 22.5 | 0.1099 | 14.7 | 0.1362 | 14.4 | 0.0911 | 25.1 | 0.1177 | 8.8 |
| 7.5 – 10 | 0.0882 | 21.7 | 0.1153 | 11.1 | 0.1592 | 10.2 | 0.1318 | 14.0 | 0.1332 | 6.4 |
| 10 – 12.5 | 0.0945 | 14.2 | 0.0910 | 9.9 | 0.1011 | 11.1 | 0.0880 | 14.1 | 0.0940 | 6.0 |
| 12.5 – 15 | 0.0638 | 19.7 | 0.0815 | 9.4 | 0.0877 | 11.1 | 0.1003 | 10.9 | 0.0868 | 5.8 |
| 15 – 20 | 0.1218 | 6.0 | 0.1152 | 4.0 | 0.1411 | 4.3 | 0.1266 | 5.3 | 0.1262 | 2.4 |
| 20 – 25 | 0.1346 | 4.3 | 0.1250 | 2.9 | 0.1298 | 3.9 | 0.1350 | 4.1 | 0.1298 | 1.8 |
| 25 – 30 | 0.1248 | 3.3 | 0.1230 | 2.2 | 0.1230 | 3.1 | 0.1228 | 3.5 | 0.1233 | 1.4 |
| 30 – 40 | 0.1417 | 2.0 | 0.1364 | 1.5 | 0.1470 | 2.0 | 0.1494 | 2.3 | 0.1420 | 0.9 |
| 40 – 50 | 0.1526 | 2.0 | 0.1512 | 1.4 | 0.1588 | 2.0 | 0.1650 | 2.2 | 0.1554 | 0.9 |
| 50 – 60 | 0.1605 | 1.9 | 0.1555 | 1.3 | 0.1584 | 1.9 | 0.1618 | 2.2 | 0.1581 | 0.9 |
| 60 – 80 | 0.1561 | 1.5 | 0.1540 | 1.2 | 0.1540 | 1.7 | 0.1543 | 2.0 | 0.1546 | 0.8 |
| 80 – 100 | 0.1632 | 1.5 | 0.1549 | 1.2 | 0.1586 | 1.7 | 0.1596 | 2.0 | 0.1584 | 0.8 |
| 100 – 120 | 0.1627 | 1.5 | 0.1567 | 1.3 | 0.1578 | 1.8 | 0.1580 | 2.2 | 0.1588 | 0.8 |
| 120 – 150 | 0.1555 | 1.4 | – | – | – | – | – | – | 0.1555 | 1.4 |
| 150 – 175 | 0.1526 | 1.5 | – | – | – | – | – | – | 0.1526 | 1.5 |
| 175 – 200 | 0.1534 | 1.6 | – | – | – | – | – | – | 0.1534 | 1.6 |
| 200 – 225 | 0.1535 | 2.2 | – | – | – | – | – | – | 0.1535 | 2.2 |
| 30 – 80 | 0.1527 | 1.3 | 0.1493 | 1.1 | 0.1546 | 1.7 | 0.1576 | 1.9 | 0.1525 | 0.7 |
| Evaluation 2 | | | | | | | | | | |
| 3 – 5 | – | – | 0.1112 | 20.6 | 0.1081 | 26.9 | 0.1199 | 25.7 | 0.1129 | 13.8 |
| 5 – 7.5 | 0.1165 | 16.9 | 0.1074 | 11.5 | 0.1369 | 11.1 | 0.1151 | 15.3 | 0.1203 | 6.6 |
| 7.5 – 10 | 0.0877 | 17.1 | 0.1415 | 7.3 | 0.1696 | 7.5 | 0.1397 | 9.8 | 0.1475 | 4.5 |
| 10 – 12.5 | 0.0797 | 13.0 | 0.1093 | 6.6 | 0.1017 | 8.6 | 0.1067 | 8.9 | 0.1037 | 4.3 |
| 12.5 – 15 | 0.0786 | 12.4 | 0.0923 | 6.5 | 0.1043 | 7.6 | 0.1100 | 7.8 | 0.0988 | 4.0 |
| 15 – 20 | 0.1328 | 4.4 | 0.1256 | 3.0 | 0.1338 | 3.6 | 0.1361 | 3.8 | 0.1311 | 1.8 |
| 20 – 25 | 0.1419 | 3.2 | 0.1376 | 2.2 | 0.1381 | 2.9 | 0.1411 | 3.1 | 0.1392 | 1.4 |
| 25 – 30 | 0.1307 | 2.5 | 0.1326 | 1.7 | 0.1268 | 2.4 | 0.1340 | 2.5 | 0.1313 | 1.1 |
| 30 – 40 | 0.1478 | 1.6 | 0.1430 | 1.2 | 0.1502 | 1.6 | 0.1495 | 1.7 | 0.1468 | 0.7 |
| 40 – 50 | 0.1546 | 1.6 | 0.1573 | 1.1 | 0.1615 | 1.5 | 0.1639 | 1.7 | 0.1588 | 0.7 |
| 50 – 60 | 0.1611 | 1.5 | 0.1579 | 1.1 | 0.1604 | 1.5 | 0.1623 | 1.7 | 0.1598 | 0.7 |
| 60 – 80 | 0.1571 | 1.2 | 0.1553 | 0.9 | 0.1540 | 1.3 | 0.1549 | 1.5 | 0.1554 | 0.6 |
| 80 –100 | 0.1612 | 1.2 | 0.1567 | 1.0 | 0.1593 | 1.3 | 0.1590 | 1.5 | 0.1587 | 0.6 |
| 100 –120 | 0.1631 | 1.2 | 0.1580 | 1.1 | 0.1559 | 1.4 | 0.1585 | 1.6 | 0.1591 | 0.6 |
| 120 –150 | 0.1555 | 1.1 | – | – | – | – | – | – | 0.1555 | 1.1 |
| 150 –175 | 0.1511 | 1.2 | – | – | – | – | – | – | 0.1511 | 1.2 |
| 175 –200 | 0.1539 | 1.3 | – | – | – | – | – | – | 0.1539 | 1.3 |
| 200 –225 | 0.1476 | 1.9 | – | – | – | – | – | – | 0.1476 | 1.9 |
| 30 – 80 | 0.1552 | 1.0 | 0.1534 | 0.9 | 0.1565 | 1.2 | 0.1577 | 1.4 | 0.1552 | 0.5 |

Table 17: $\sigma(^{145}\mathrm{Nd})/\sigma(^{197}\mathrm{Au})$ AND STATISTICAL UNCERTAINTIES IN (%)

| Energy Bin (keV) | Run I | | Run II | | Run III | | Run IV | | Average | |
|---|---|---|---|---|---|---|---|---|---|---|
| Evaluation 1 | | | | | | | | | | |
| 3 – 5 | 0.6826 | 12.1 | 0.6274 | 9.5 | 0.8003 | 8.9 | 0.5566 | 12.1 | 0.6832 | 5.2 |
| 5 – 7.5 | 0.7630 | 7.3 | 0.6653 | 5.6 | 0.7412 | 5.5 | 0.7120 | 6.5 | 0.7162 | 3.1 |
| 7.5 – 10 | 0.8015 | 5.9 | 0.7100 | 4.6 | 0.7287 | 5.0 | 0.7480 | 5.5 | 0.7413 | 2.6 |
| 10 – 12.5 | 0.6740 | 4.9 | 0.6957 | 3.6 | 0.6524 | 4.0 | 0.6726 | 4.3 | 0.6752 | 2.1 |
| 12.5 – 15 | 0.8109 | 4.2 | 0.7184 | 3.1 | 0.7794 | 3.2 | 0.7564 | 3.6 | 0.7602 | 1.7 |
| 15 – 20 | 0.7556 | 2.6 | 0.7828 | 1.8 | 0.7918 | 2.0 | 0.7859 | 2.3 | 0.7815 | 1.1 |
| 20 – 25 | 0.7839 | 2.1 | 0.8074 | 1.5 | 0.8263 | 1.8 | 0.8160 | 2.0 | 0.8100 | 0.9 |
| 25 – 30 | 0.7565 | 1.7 | 0.7664 | 1.2 | 0.7817 | 1.5 | 0.7788 | 1.7 | 0.7708 | 0.7 |
| 30 – 40 | 0.7361 | 1.3 | 0.7446 | 1.0 | 0.7453 | 1.1 | 0.7632 | 1.3 | 0.7466 | 0.6 |
| 40 – 50 | 0.7541 | 1.3 | 0.7607 | 1.0 | 0.7740 | 1.1 | 0.7905 | 1.3 | 0.7684 | 0.6 |
| 50 – 60 | 0.7355 | 1.3 | 0.7349 | 1.0 | 0.7526 | 1.1 | 0.7643 | 1.3 | 0.7452 | 0.6 |
| 60 – 80 | 0.6958 | 1.1 | 0.7053 | 0.8 | 0.7036 | 1.0 | 0.7145 | 1.1 | 0.7046 | 0.5 |
| 80 – 100 | 0.6409 | 1.1 | 0.6409 | 0.9 | 0.6506 | 1.0 | 0.6529 | 1.2 | 0.6456 | 0.5 |
| 100 – 120 | 0.5885 | 1.1 | 0.6026 | 0.9 | 0.6076 | 1.1 | 0.6156 | 1.3 | 0.6028 | 0.6 |
| 120 – 150 | 0.5582 | 1.1 | – | – | – | – | – | – | 0.5582 | 1.1 |
| 150 – 175 | 0.5340 | 1.1 | – | – | – | – | – | – | 0.5340 | 1.1 |
| 175 – 200 | 0.5213 | 1.2 | – | – | – | – | – | – | 0.5213 | 1.2 |
| 200 – 225 | 0.4909 | 1.7 | – | – | – | – | – | – | 0.4909 | 1.7 |
| 30 – 80 | 0.7304 | 1.1 | 0.7364 | 1.0 | 0.7439 | 1.1 | 0.7581 | 1.3 | 0.7412 | 0.6 |
| Evaluation 2 | | | | | | | | | | |
| 3 – 5 | 0.8031 | 8.5 | 0.6615 | 6.6 | 0.7854 | 6.6 | 0.6769 | 7.9 | 0.7284 | 3.7 |
| 5 – 7.5 | 0.7687 | 5.5 | 0.6943 | 3.9 | 0.7581 | 4.0 | 0.7477 | 4.8 | 0.7375 | 2.2 |
| 7.5 – 10 | 0.7888 | 4.6 | 0.7514 | 3.3 | 0.7738 | 3.5 | 0.7665 | 4.0 | 0.7676 | 1.9 |
| 10 – 12.5 | 0.7022 | 3.7 | 0.7198 | 2.6 | 0.7003 | 2.9 | 0.7200 | 3.2 | 0.7115 | 1.5 |
| 12.5 – 15 | 0.8272 | 3.2 | 0.7464 | 2.3 | 0.7841 | 2.5 | 0.7790 | 2.8 | 0.7776 | 1.3 |
| 15 – 20 | 0.7744 | 2.0 | 0.8017 | 1.4 | 0.8055 | 1.6 | 0.8203 | 1.8 | 0.8023 | 0.8 |
| 20 – 25 | 0.8075 | 1.7 | 0.8162 | 1.2 | 0.8314 | 1.4 | 0.8295 | 1.6 | 0.8213 | 0.7 |
| 25 – 30 | 0.7684 | 1.4 | 0.7771 | 1.0 | 0.7810 | 1.2 | 0.7810 | 1.4 | 0.7771 | 0.6 |
| 30 – 40 | 0.7522 | 1.0 | 0.7490 | 0.8 | 0.7492 | 0.9 | 0.7759 | 1.1 | 0.7548 | 0.5 |
| 40 – 50 | 0.7568 | 1.1 | 0.7644 | 0.8 | 0.7790 | 1.0 | 0.7917 | 1.1 | 0.7715 | 0.5 |
| 50 – 60 | 0.7387 | 1.1 | 0.7360 | 0.8 | 0.7509 | 1.0 | 0.7644 | 1.1 | 0.7456 | 0.5 |
| 60 – 80 | 0.6989 | 0.9 | 0.7014 | 0.7 | 0.7049 | 0.8 | 0.7187 | 1.0 | 0.7049 | 0.4 |
| 80 –100 | 0.6410 | 0.9 | 0.6380 | 0.7 | 0.6489 | 0.8 | 0.6548 | 1.0 | 0.6444 | 0.4 |
| 100 –120 | 0.5879 | 1.0 | 0.5957 | 0.8 | 0.6036 | 0.9 | 0.6103 | 1.2 | 0.5985 | 0.5 |
| 120 –150 | 0.5571 | 0.9 | – | – | – | – | – | – | 0.5571 | 0.9 |
| 150 –175 | 0.5306 | 1.0 | – | – | – | – | – | – | 0.5306 | 1.0 |
| 175 –200 | 0.5178 | 1.0 | – | – | – | – | – | – | 0.5178 | 1.0 |
| 200 –225 | 0.4901 | 1.5 | – | – | – | – | – | – | 0.4901 | 1.5 |
| 30 – 80 | 0.7367 | 0.9 | 0.7377 | 0.8 | 0.7460 | 0.9 | 0.7627 | 1.0 | 0.7442 | 0.4 |

Table 18: $\sigma(^{146}\mathrm{Nd})/\sigma(^{197}\mathrm{Au})$ AND STATISTICAL UNCERTAINTIES IN (%)

| Energy Bin (keV) | Run I | | Run II | | Run III | | Run IV | | Average | |
|---|---|---|---|---|---|---|---|---|---|---|
| Evaluation 1 | | | | | | | | | | |
| 3 – 5 | 0.0961 | 41.7 | 0.0618 | 46.8 | 0.0617 | 63.4 | 0.0000 | – | 0.0772 | 28.6 |
| 5 – 7.5 | 0.1297 | 18.4 | 0.1315 | 12.4 | 0.1422 | 14.5 | 0.0701 | 33.2 | 0.1309 | 8.2 |
| 7.5 – 10 | 0.0841 | 21.6 | 0.1218 | 10.6 | 0.1221 | 13.8 | 0.1026 | 18.4 | 0.1147 | 7.3 |
| 10 – 12.5 | 0.0954 | 13.5 | 0.1065 | 8.6 | 0.1122 | 10.5 | 0.1092 | 11.8 | 0.1068 | 5.3 |
| 12.5 – 15 | 0.1407 | 8.8 | 0.1370 | 5.8 | 0.1551 | 6.8 | 0.1429 | 8.0 | 0.1437 | 3.5 |
| 15 – 20 | 0.1380 | 5.1 | 0.1211 | 3.8 | 0.1297 | 4.8 | 0.1229 | 5.5 | 0.1269 | 2.3 |
| 20 – 25 | 0.1701 | 3.4 | 0.1672 | 2.3 | 0.1567 | 3.4 | 0.1563 | 3.7 | 0.1639 | 1.5 |
| 25 – 30 | 0.1634 | 2.6 | 0.1667 | 1.8 | 0.1532 | 2.8 | 0.1508 | 3.1 | 0.1610 | 1.2 |
| 30 – 40 | 0.1631 | 1.8 | 0.1658 | 1.4 | 0.1717 | 1.9 | 0.1738 | 2.1 | 0.1677 | 0.9 |
| 40 – 50 | 0.1647 | 1.8 | 0.1633 | 1.4 | 0.1687 | 2.0 | 0.1688 | 2.2 | 0.1656 | 0.9 |
| 50 – 60 | 0.1870 | 1.7 | 0.1848 | 1.2 | 0.1818 | 1.8 | 0.1846 | 2.1 | 0.1847 | 0.8 |
| 60 – 80 | 0.1831 | 1.3 | 0.1842 | 1.1 | 0.1788 | 1.6 | 0.1807 | 1.8 | 0.1824 | 0.7 |
| 80 – 100 | 0.1959 | 1.3 | 0.1951 | 1.1 | 0.1963 | 1.6 | 0.1948 | 1.9 | 0.1955 | 0.7 |
| 100 – 120 | 0.2009 | 1.3 | 0.1987 | 1.2 | 0.1958 | 1.7 | 0.1944 | 2.0 | 0.1983 | 0.7 |
| 120 – 150 | 0.1911 | 1.2 | – | – | – | – | – | – | 0.1911 | 1.2 |
| 150 – 175 | 0.1959 | 1.3 | – | – | – | – | – | – | 0.1959 | 1.3 |
| 175 – 200 | 0.1917 | 1.3 | – | – | – | – | – | – | 0.1917 | 1.3 |
| 200 – 225 | 0.1969 | 1.9 | – | – | – | – | – | – | 0.1969 | 1.9 |
| 30 – 80 | 0.1745 | 1.1 | 0.1745 | 1.1 | 0.1753 | 1.5 | 0.1770 | 1.8 | 0.1751 | 0.6 |
| Evaluation 2 | | | | | | | | | | |
| 3 – 5 | 0.0791 | 40.8 | 0.0683 | 34.7 | 0.1153 | 26.3 | – | – | 0.0942 | 19.1 |
| 5 – 7.5 | 0.1173 | 15.5 | 0.1149 | 11.2 | 0.1389 | 11.2 | 0.0862 | 20.9 | 0.1209 | 6.8 |
| 7.5 – 10 | 0.0870 | 16.0 | 0.1185 | 8.9 | 0.1382 | 9.3 | 0.1089 | 12.9 | 0.1199 | 5.5 |
| 10 – 12.5 | 0.1013 | 9.6 | 0.1140 | 6.5 | 0.1204 | 7.4 | 0.1062 | 9.2 | 0.1122 | 4.0 |
| 12.5 – 15 | 0.1460 | 6.4 | 0.1424 | 4.5 | 0.1632 | 5.0 | 0.1460 | 6.1 | 0.1495 | 2.7 |
| 15 – 20 | 0.1326 | 4.1 | 0.1288 | 2.9 | 0.1340 | 3.6 | 0.1294 | 4.0 | 0.1309 | 1.8 |
| 20 – 25 | 0.1767 | 2.5 | 0.1725 | 1.8 | 0.1641 | 2.5 | 0.1613 | 2.8 | 0.1696 | 1.2 |
| 25 – 30 | 0.1651 | 2.0 | 0.1657 | 1.5 | 0.1556 | 2.1 | 0.1574 | 2.3 | 0.1621 | 0.9 |
| 30 – 40 | 0.1676 | 1.4 | 0.1677 | 1.1 | 0.1709 | 1.5 | 0.1754 | 1.6 | 0.1697 | 0.7 |
| 40 – 50 | 0.1655 | 1.4 | 0.1666 | 1.1 | 0.1706 | 1.5 | 0.1701 | 1.6 | 0.1678 | 0.7 |
| 50 – 60 | 0.1870 | 1.3 | 0.1843 | 1.0 | 0.1845 | 1.4 | 0.1873 | 1.5 | 0.1855 | 0.6 |
| 60 – 80 | 0.1845 | 1.1 | 0.1843 | 0.9 | 0.1785 | 1.2 | 0.1838 | 1.3 | 0.1831 | 0.5 |
| 80 –100 | 0.1945 | 1.0 | 0.1941 | 0.9 | 0.1937 | 1.2 | 0.1956 | 1.4 | 0.1944 | 0.5 |
| 100 –120 | 0.2001 | 1.0 | 0.1978 | 1.0 | 0.1924 | 1.3 | 0.1950 | 1.5 | 0.1971 | 0.6 |
| 120 –150 | 0.1901 | 1.0 | – | – | – | – | – | – | 0.1901 | 1.0 |
| 150 –175 | 0.1936 | 1.0 | – | – | – | – | – | – | 0.1936 | 1.0 |
| 175 –200 | 0.1919 | 1.1 | – | – | – | – | – | – | 0.1919 | 1.1 |
| 200 –225 | 0.1937 | 1.6 | – | – | – | – | – | – | 0.1937 | 1.6 |
| 30 – 80 | 0.1762 | 0.8 | 0.1757 | 0.8 | 0.1761 | 1.1 | 0.1792 | 1.3 | 0.1765 | 0.5 |

Table 19: $\sigma(^{148}\mathrm{Nd})/\sigma(^{197}\mathrm{Au})$ AND STATISTICAL UNCERTAINTIES IN (%)

| Energy Bin (keV) | Run I | | Run II | | Run III | | Run IV | | Average | |
|---|---|---|---|---|---|---|---|---|---|---|
| Evaluation 1 | | | | | | | | | | |
| 3 – 5 | 0.1101 | 46.2 | 0.1230 | 32.6 | 0.1803 | 29.9 | 0.0530 | 98.5 | 0.1423 | 20.1 |
| 5 – 7.5 | 0.1804 | 17.0 | 0.1402 | 15.9 | 0.1885 | 14.9 | 0.0988 | 30.4 | 0.1641 | 8.9 |
| 7.5 – 10 | 0.1704 | 13.9 | 0.1484 | 11.9 | 0.2230 | 10.5 | 0.1802 | 13.6 | 0.1844 | 6.2 |
| 10 – 12.5 | 0.2088 | 8.2 | 0.2158 | 6.0 | 0.2104 | 7.8 | 0.2576 | 6.7 | 0.2249 | 3.5 |
| 12.5 – 15 | 0.2205 | 7.4 | 0.2158 | 5.0 | 0.2073 | 6.8 | 0.2327 | 6.4 | 0.2189 | 3.1 |
| 15 – 20 | 0.2229 | 4.2 | 0.2214 | 2.9 | 0.2301 | 3.7 | 0.2327 | 3.8 | 0.2261 | 1.8 |
| 20 – 25 | 0.2365 | 3.1 | 0.2440 | 2.1 | 0.2412 | 3.0 | 0.2570 | 2.9 | 0.2448 | 1.3 |
| 25 – 30 | 0.2384 | 2.3 | 0.2342 | 1.7 | 0.2441 | 2.3 | 0.2379 | 2.5 | 0.2379 | 1.1 |
| 30 – 40 | 0.2389 | 1.6 | 0.2319 | 1.3 | 0.2394 | 1.7 | 0.2456 | 1.7 | 0.2378 | 0.8 |
| 40 – 50 | 0.2610 | 1.5 | 0.2522 | 1.2 | 0.2632 | 1.6 | 0.2714 | 1.7 | 0.2603 | 0.7 |
| 50 – 60 | 0.2841 | 1.4 | 0.2767 | 1.1 | 0.2772 | 1.6 | 0.2938 | 1.6 | 0.2818 | 0.7 |
| 60 – 80 | 0.2945 | 1.1 | 0.2901 | 0.9 | 0.2916 | 1.3 | 0.2980 | 1.3 | 0.2930 | 0.6 |
| 80 – 100 | 0.3007 | 1.1 | 0.3009 | 1.0 | 0.2984 | 1.3 | 0.3036 | 1.4 | 0.3009 | 0.6 |
| 100 – 120 | 0.3287 | 1.1 | 0.3169 | 1.0 | 0.3216 | 1.4 | 0.3212 | 1.5 | 0.3222 | 0.6 |
| 120 – 150 | 0.3108 | 1.0 | – | – | – | – | – | – | 0.3108 | 1.0 |
| 150 – 175 | 0.3077 | 1.1 | – | – | – | – | – | – | 0.3077 | 1.1 |
| 175 – 200 | 0.2998 | 1.2 | – | – | – | – | – | – | 0.2998 | 1.2 |
| 200 – 225 | 0.3045 | 1.7 | – | – | – | – | – | – | 0.3045 | 1.7 |
| 30 – 80 | 0.2696 | 0.9 | 0.2627 | 1.0 | 0.2679 | 1.3 | 0.2772 | 1.4 | 0.2682 | 0.5 |
| Evaluation 2 | | | | | | | | | | |
| 3 – 5 | 0.1400 | 28.1 | 0.1650 | 17.9 | 0.1855 | 21.0 | 0.1406 | 26.5 | 0.1625 | 11.2 |
| 5 – 7.5 | 0.1981 | 11.3 | 0.1633 | 9.8 | 0.1863 | 10.8 | 0.1645 | 13.0 | 0.1778 | 5.6 |
| 7.5 – 10 | 0.1782 | 9.7 | 0.1985 | 6.7 | 0.2325 | 7.3 | 0.2049 | 8.3 | 0.2064 | 3.9 |
| 10 – 12.5 | 0.2314 | 5.4 | 0.2362 | 4.1 | 0.2156 | 5.5 | 0.2515 | 4.9 | 0.2350 | 2.4 |
| 12.5 – 15 | 0.2457 | 4.8 | 0.2361 | 3.4 | 0.2409 | 4.4 | 0.2476 | 4.4 | 0.2415 | 2.1 |
| 15 – 20 | 0.2395 | 2.9 | 0.2378 | 2.1 | 0.2307 | 2.7 | 0.2416 | 2.7 | 0.2374 | 1.3 |
| 20 – 25 | 0.2515 | 2.2 | 0.2508 | 1.6 | 0.2504 | 2.2 | 0.2555 | 2.2 | 0.2518 | 1.0 |
| 25 – 30 | 0.2402 | 1.7 | 0.2404 | 1.3 | 0.2431 | 1.7 | 0.2402 | 1.8 | 0.2409 | 0.8 |
| 30 – 40 | 0.2412 | 1.2 | 0.2361 | 0.9 | 0.2382 | 1.3 | 0.2404 | 1.3 | 0.2384 | 0.6 |
| 40 – 50 | 0.2638 | 1.2 | 0.2580 | 0.9 | 0.2650 | 1.2 | 0.2654 | 1.3 | 0.2621 | 0.6 |
| 50 – 60 | 0.2821 | 1.2 | 0.2799 | 0.8 | 0.2764 | 1.2 | 0.2857 | 1.2 | 0.2808 | 0.5 |
| 60 – 80 | 0.2933 | 0.9 | 0.2906 | 0.7 | 0.2888 | 1.0 | 0.2924 | 1.0 | 0.2912 | 0.4 |
| 80 –100 | 0.2977 | 0.9 | 0.2993 | 0.7 | 0.2934 | 1.0 | 0.2942 | 1.0 | 0.2970 | 0.4 |
| 100 –120 | 0.3262 | 0.9 | 0.3171 | 0.8 | 0.3156 | 1.1 | 0.3118 | 1.2 | 0.3186 | 0.5 |
| 120 –150 | 0.3068 | 0.8 | – | – | – | – | – | – | 0.3068 | 0.8 |
| 150 –175 | 0.3025 | 0.9 | – | – | – | – | – | – | 0.3025 | 0.9 |
| 175 –200 | 0.2976 | 1.0 | – | – | – | – | – | – | 0.2976 | 1.0 |
| 200 –225 | 0.2988 | 1.4 | – | – | – | – | – | – | 0.2988 | 1.4 |
| 30 – 80 | 0.2701 | 0.7 | 0.2662 | 0.7 | 0.2671 | 0.9 | 0.2710 | 1.0 | 0.2681 | 0.4 |

Table 20: FINAL NEUTRON CAPTURE CROSS SECTION RATIOS OF $^{142}$Nd, $^{143}$Nd, $^{144}$Nd, $^{145}$Nd $^{146}$Nd, AND $^{148}$Nd RELATIVE TO $^{197}$Au

| Energy[1] | $\frac{\sigma(^{142}\mathrm{Nd})}{\sigma(^{197}\mathrm{Au})}$ | Uncertainty (%) | | | $\frac{\sigma(^{143}\mathrm{Nd})}{\sigma(^{197}\mathrm{Au})}$ | Uncertainty (%) | | | $\frac{\sigma(^{144}\mathrm{Nd})}{\sigma(^{197}\mathrm{Au})}$ | Uncertainty (%) | | |
|---|---|---|---|---|---|---|---|---|---|---|---|---|
| (keV) | | stat | sys | tot | | stat | sys | tot | | stat | sys | tot |
| 3 – 5 | 0.0330 | 33.3 | 1.9 | 33.4 | 0.4470 | 4.4 | 1.4 | 4.6 | 0.1129 | 13.8 | 1.7 | 13.9 |
| 5 – 7.5 | 0.0538 | 9.7 | 1.9 | 9.9 | 0.4358 | 2.8 | 1.4 | 3.1 | 0.1203 | 6.6 | 1.7 | 6.8 |
| 7.5 – 10 | 0.0661 | 6.6 | 1.9 | 6.9 | 0.4437 | 2.4 | 1.4 | 2.8 | 0.1475 | 4.5 | 1.7 | 4.8 |
| 10 – 12.5 | 0.0392 | 8.1 | 1.9 | 8.3 | 0.4031 | 2.0 | 1.4 | 2.4 | 0.1037 | 4.3 | 1.7 | 4.6 |
| 12.5 – 15 | 0.0708 | 4.1 | 1.9 | 4.5 | 0.4545 | 1.7 | 1.4 | 2.2 | 0.0988 | 4.0 | 1.7 | 4.3 |
| 15 – 20 | 0.0474 | 3.7 | 1.9 | 4.2 | 0.4348 | 1.1 | 1.4 | 1.8 | 0.1311 | 1.8 | 1.7 | 2.5 |
| 20 – 25 | 0.0695 | 2.1 | 1.9 | 2.8 | 0.4680 | 0.9 | 1.4 | 1.7 | 0.1392 | 1.4 | 1.7 | 2.2 |
| 25 – 30 | 0.0500 | 2.0 | 1.9 | 2.8 | 0.4497 | 0.7 | 1.4 | 1.6 | 0.1313 | 1.1 | 1.7 | 2.0 |
| 30 – 40 | 0.0631 | 1.2 | 1.9 | 2.2 | 0.4222 | 0.5 | 1.4 | 1.5 | 0.1468 | 0.7 | 1.7 | 1.8 |
| 40 – 50 | 0.0633 | 1.2 | 1.9 | 2.2 | 0.4204 | 0.6 | 1.4 | 1.5 | 0.1588 | 0.7 | 1.7 | 1.8 |
| 50 – 60 | 0.0652 | 1.1 | 1.9 | 2.2 | 0.4059 | 0.6 | 1.4 | 1.5 | 0.1598 | 0.7 | 1.7 | 1.8 |
| 60 – 80 | 0.0663 | 0.9 | 1.9 | 2.1 | 0.4033 | 0.4 | 1.4 | 1.5 | 0.1554 | 0.6 | 1.7 | 1.8 |
| 80 – 100 | 0.0634 | 1.0 | 1.9 | 2.1 | 0.3884 | 0.5 | 1.4 | 1.5 | 0.1587 | 0.6 | 1.7 | 1.8 |
| 100 – 120 | 0.0629 | 1.0 | 1.9 | 2.1 | 0.3800 | 0.5 | 1.4 | 1.5 | 0.1591 | 0.6 | 1.7 | 1.8 |
| 120 – 150 | 0.0669 | 1.8 | 1.9 | 2.6 | 0.3606 | 1.0 | 1.4 | 1.7 | 0.1555 | 1.1 | 1.7 | 2.0 |
| 150 – 175 | 0.0618 | 1.9 | 1.9 | 2.7 | 0.3462 | 1.1 | 1.4 | 1.8 | 0.1511 | 1.2 | 1.7 | 2.1 |
| 175 – 200 | 0.0650 | 1.9 | 1.9 | 2.7 | 0.3443 | 1.1 | 1.4 | 1.8 | 0.1539 | 1.3 | 1.7 | 2.1 |
| 200 – 225 | 0.0612 | 2.8 | 1.9 | 3.4 | 0.3353 | 1.6 | 1.4 | 2.1 | 0.1476 | 1.9 | 1.7 | 2.5 |

| Energy [1] | $\frac{\sigma(^{145}\mathrm{Nd})}{\sigma(^{197}\mathrm{Au})}$ | Uncertainty (%) | | | $\frac{\sigma(^{146}\mathrm{Nd})}{\sigma(^{197}\mathrm{Au})}$ | Uncertainty (%) | | | $\frac{\sigma(^{148}\mathrm{Nd})}{\sigma(^{197}\mathrm{Au})}$ | Uncertainty (%) | | |
|---|---|---|---|---|---|---|---|---|---|---|---|---|
| (keV) | | stat | sys | tot | | stat | sys | tot | | stat | sys | tot |
| 3 – 5 | 0.7284 | 3.7 | 1.3 | 3.9 | 0.0942 | 19.1 | 1.4 | 19.2 | 0.1625 | 11.2 | 1.5 | 11.3 |
| 5 – 7.5 | 0.7375 | 2.2 | 1.3 | 2.6 | 0.1209 | 6.8 | 1.4 | 6.9 | 0.1778 | 5.6 | 1.5 | 5.8 |
| 7.5 – 10 | 0.7676 | 1.9 | 1.3 | 2.3 | 0.1199 | 5.5 | 1.4 | 5.7 | 0.2064 | 3.9 | 1.5 | 4.2 |
| 10 –12.5 | 0.7115 | 1.5 | 1.3 | 2.0 | 0.1122 | 4.0 | 1.4 | 4.2 | 0.2350 | 2.4 | 1.5 | 2.8 |
| 12.5 – 15 | 0.7776 | 1.3 | 1.3 | 1.8 | 0.1495 | 2.7 | 1.4 | 3.0 | 0.2415 | 2.1 | 1.5 | 2.6 |
| 15 – 20 | 0.8023 | 0.8 | 1.3 | 1.5 | 0.1309 | 1.8 | 1.4 | 2.3 | 0.2374 | 1.3 | 1.5 | 2.0 |
| 20 – 25 | 0.8213 | 0.7 | 1.3 | 1.5 | 0.1696 | 1.2 | 1.4 | 1.8 | 0.2518 | 1.0 | 1.5 | 1.8 |
| 25 – 30 | 0.7771 | 0.6 | 1.3 | 1.4 | 0.1621 | 0.9 | 1.4 | 1.7 | 0.2409 | 0.8 | 1.5 | 1.7 |
| 30 – 40 | 0.7548 | 0.5 | 1.3 | 1.4 | 0.1697 | 0.7 | 1.4 | 1.6 | 0.2384 | 0.6 | 1.5 | 1.6 |
| 40 – 50 | 0.7715 | 0.5 | 1.3 | 1.4 | 0.1678 | 0.7 | 1.4 | 1.6 | 0.2621 | 0.6 | 1.5 | 1.6 |
| 50 – 60 | 0.7456 | 0.5 | 1.3 | 1.4 | 0.1855 | 0.6 | 1.4 | 1.5 | 0.2808 | 0.5 | 1.5 | 1.6 |
| 60 – 80 | 0.7049 | 0.4 | 1.3 | 1.4 | 0.1831 | 0.5 | 1.4 | 1.5 | 0.2912 | 0.4 | 1.5 | 1.6 |
| 80 – 100 | 0.6444 | 0.4 | 1.3 | 1.4 | 0.1944 | 0.5 | 1.4 | 1.5 | 0.2970 | 0.4 | 1.5 | 1.6 |
| 100 – 120 | 0.5985 | 0.5 | 1.3 | 1.4 | 0.1971 | 0.6 | 1.4 | 1.5 | 0.3186 | 0.5 | 1.5 | 1.6 |
| 120 – 150 | 0.5571 | 0.9 | 1.3 | 1.6 | 0.1901 | 1.0 | 1.4 | 1.7 | 0.3068 | 0.8 | 1.5 | 1.7 |
| 150 – 175 | 0.5306 | 1.0 | 1.3 | 1.6 | 0.1936 | 1.0 | 1.4 | 1.7 | 0.3025 | 0.9 | 1.5 | 1.7 |
| 175 – 200 | 0.5178 | 1.0 | 1.3 | 1.6 | 0.1919 | 1.1 | 1.4 | 1.8 | 0.2976 | 1.0 | 1.5 | 1.8 |
| 200 – 225 | 0.4901 | 1.5 | 1.3 | 2.0 | 0.1937 | 1.6 | 1.4 | 2.1 | 0.2988 | 1.4 | 1.5 | 2.1 |

[1] Neutron energy intervals as used for calculating the Maxwellian averaged cross sections

Figure 15: The neutron capture cross sections of $^{142}$Nd and $^{143}$Nd compared to the data of Mathews and Käppeler [9].

Figure 16: The neutron capture cross sections of $^{144}$Nd and $^{145}$Nd compared to the data of Mathews and Käppeler [9] for $^{144}$Nd.

Figure 17: The neutron capture cross sections of $^{146}$Nd and $^{148}$Nd.

Table 21: NEUTRON CAPTURE CROSS SECTIONS OF $^{142}$Nd, $^{143}$Nd,$^{144}$Nd, $^{145}$Nd, $^{146}$Nd, AND $^{148}$Nd (in mb)

| Energy bin[1] (keV) | $\sigma(^{197}\mathrm{Au})^2$ | $\sigma(^{142}\mathrm{Nd})$ | $\sigma(^{143}\mathrm{Nd})$ | $\sigma(^{144}\mathrm{Nd})$ | $\sigma(^{145}\mathrm{Nd})$ | $\sigma(^{146}\mathrm{Nd})$ | $\sigma(^{148}\mathrm{Nd})$ |
|---|---|---|---|---|---|---|---|
| 3 – 5 | 2266.7 | 74.7 | 1013. | 255.9 | 1651. | 213.5 | 368.4 |
| 5 – 7.5 | 1726.7 | 93.0 | 752.6 | 207.8 | 1273. | 208.7 | 307.0 |
| 7.5 – 10 | 1215.7 | 80.4 | 539.4 | 179.3 | 933.2 | 145.8 | 250.9 |
| 10 – 12.5 | 1066.7 | 41.8 | 430.0 | 110.6 | 759.0 | 119.7 | 250.7 |
| 12.5 – 15 | 878.0 | 62.2 | 399.0 | 86.7 | 682.7 | 131.3 | 212.0 |
| 15 – 20 | 738.8 | 35.0 | 321.2 | 96.9 | 592.7 | 96.7 | 175.4 |
| 20 – 25 | 600.0 | 41.7 | 280.8 | 83.5 | 492.8 | 101.8 | 151.1 |
| 25 – 30 | 570.8 | 28.6 | 256.7 | 75.0 | 443.6 | 92.5 | 137.5 |
| 30 – 40 | 500.4 | 31.6 | 211.3 | 73.5 | 377.7 | 84.9 | 119.3 |
| 40 – 50 | 433.3 | 27.5 | 182.2 | 68.8 | 334.3 | 72.7 | 113.6 |
| 50 – 60 | 389.6 | 25.4 | 158.1 | 62.3 | 290.5 | 72.3 | 109.4 |
| 60 – 80 | 349.4 | 23.2 | 140.9 | 54.3 | 246.3 | 64.0 | 101.7 |
| 80 – 100 | 298.3 | 18.9 | 115.9 | 47.4 | 192.2 | 58.0 | 88.6 |
| 100 – 120 | 290.1 | 18.3 | 110.3 | 46.2 | 173.6 | 57.2 | 92.4 |
| 120 – 150 | 274.1 | 18.3 | 98.8 | 42.6 | 152.7 | 52.1 | 84.1 |
| 150 – 175 | 263.7 | 16.3 | 91.3 | 39.8 | 139.9 | 51.1 | 79.7 |
| 175 – 200 | 252.6 | 16.4 | 87.0 | 38.9 | 130.8 | 48.5 | 75.2 |
| 200 – 225 | 248.5 | 15.2 | 83.3 | 36.7 | 121.8 | 48.1 | 74.2 |

[1] as used for calculating the Maxwellian averaged cross sections
[2] based on the $^{197}$Au data from literature [37, 38]

# 5 DISCUSSION OF UNCERTAINTIES

The determination of statistical and systematic uncertainties in measurements with the $4\pi$ $BaF_2$ detector has been described in Refs. [21, 22, 24]. The following discussion concentrates on the particular aspects of the present experiment. The various uncertainties are compiled in Table 22.

The binding energy for all neodymium isotopes is sufficiently low to allow a proper normalization of the scattering background in the sum–energy region around 9 MeV. Therefore, no systematic differences were observed in the data, neither between individual runs nor correlated with the different acquisition modes, evaluation methods or scattering samples (see Tables 14 to 19). This implies that the systematic uncertainty for background subtraction was negligible as in case of the measurements on the samarium [22] and

gadolinium [20] isotopes. This result could be confirmed via the pulse height spectra measured at low neutron energies. The absence of any (positive or negative) structure around 9 MeV $\gamma$–ray energy due to neutron captures in the odd barium isotopes clearly demonstrates the correct treatment of the scattering background.

The systematic uncertainties due to the flight path and the neutron flux normalization have been discussed in previous work and are given in Table 22.

So far, sample impurities by other elements have been checked by spectroscopic analyses and were always found to be low enough not to affect the results. Though such contaminations by other rare earth elements are more likely due to their chemical similarity, the previous experiments on samarium and gadolinium isotopes were not hampered by this background. The case of the neodymium isotopes is more critical, however, since the cross sections of $^{142}$Nd and $^{151}$Eu differ by a factor of 130! Thus even tiny Eu admixtures may cause significant corrections. The elemental impurities specified for the $^{142}$Nd sample were, for example, Pb (0.11%), Pr (0.10%), Eu (0.04%), Sm (0.16%), and Ce (0.44%).

In view of their importance, these impurities have been carefully measured by neutron activation analysis and were found to be much smaller than originally specified. In fact, it turned out that the related corrections were completely negligible. A detailed description of these measurements will be given elsewhere [39].

The isotopic composition, as redetermined at IPPE after the experiment (see Table 2), was specified with an absolute uncertainty of <0.2% for the main isotope in each sample. This seems to be a conservative estimate according to the very good agreement with the independent measurements at FZK. Nevertheless, the values specified by the IPPE were adopted in the analysis, which means that uncertainties of 0.2% were attributed to the sample masses of $^{142}$Nd, $^{144}$Nd, and $^{146}$Nd, while the uncertainties of the $^{145}$Nd, $^{148}$Nd samples were 0.3%, and that of $^{143}$Nd was 0.4%.

The isotopic impurites were determined with an uncertainty of <0.1%. Nevertheless, the uncertainty of the isotopic correction may be much larger due to the cross section differences between even and odd isotopes of up to a factor of ten. Though reduced *effective* cross sections were used for the impurities, which account for the higher binding energies, relatively large uncertainties of 0.4% and 0.3% had to be considered due to the respective $^{143}$Nd and $^{145}$Nd impurities in the $^{142}$Nd and $^{144}$Nd samples. Renormalization of this correction for avoiding an overcompensation in the $^{144}$Nd sample caused a 2% change in the cross section. If a 30% uncertainty is assumed for the renormalization, this correction contributes a final uncertainty of 0.7% for the $^{144}$Nd sample. For all other samples, an uncertainty of 0.2% was obtained, comparable to the corrections determined in previous work.

The samples with low enrichment are also problematic with respect to the correction for multiple scattering and self–shielding. Subtraction of the normalized spectra of the impurity isotopes may either be insufficient or may even overcompensate the multiple scattering effect as in the above example of the $^{145}$Nd impurity in the $^{144}$Nd sample. Therefore, the calculation of the correction factors MS was performed twice, before and after the correction for isotopic impurities. The respective differences were ~2% for the $^{143}$Nd, $^{144}$Nd, $^{148}$Nd samples, and ~1% for the $^{145}$Nd sample, nearly independent of the neutron energy. In analogy to the gadolinium experiment [20], 25% of this difference

Table 22: SYSTEMATIC UNCERTAINTIES (%)

| | |
|---|---|
| Flight path | 0.1 |
| Neutron flux normalization | 0.2 |
| Sample mass: elemental impurities ($^{142}$Nd/other samples) | 1.5/1.0 |
| Isotopic composition ($^{143}$Nd/$^{145}$Nd,$^{148}$Nd/other samples) | 0.4/0.3/0.2 |
| Isotopic correction ($^{142}$Nd/$^{144}$Nd/other samples) | 0.4/0.7/0.2 |
| Multiple scattering and self–shielding: $F_2$ | |
| cross section ratio $^{142,143,144}$Nd/Au | 0.8/0.7/0.9 |
| cross section ratio $^{145,146,148}$Nd/Au | 0.4/0.6/0.8 |
| Undetected events: $F_1$ | |
| cross section ratio | 0.6 |
| total systematic uncertainties | |
| $\sigma(^{142}\mathrm{Nd})/\sigma(\mathrm{Au})$ | 1.9 |
| $\sigma(^{143}\mathrm{Nd})/\sigma(\mathrm{Au})$ | 1.4 |
| $\sigma(^{144}\mathrm{Nd})/\sigma(\mathrm{Au})$ | 1.7 |
| $\sigma(^{145}\mathrm{Nd})/\sigma(\mathrm{Au})$ | 1.3 |
| $\sigma(^{146}\mathrm{Nd})/\sigma(\mathrm{Au})$ | 1.4 |
| $\sigma(^{148}\mathrm{Nd})/\sigma(\mathrm{Au})$ | 1.5 |

were adopted for the related systematic uncertainty. For the other isotopes, only the uncertainties provided by the SESH code [26] were considered. This was justified by the fact that the measured total and capture cross sections could be reproduced in these calculations.

The systematic uncertainties due to the fraction of events below the detection threshold have been discussed in detail for the gadolinium experiment [20], where uncertainties of 0.3% for the even and 0.8% for the odd isotopes were estimated for the correction factor $F_1$. This estimate was based on two independent sets of calculated capture cascades, and was found to agree well with the respective uncertainties quoted in previous measurements with the $4\pi$ $BaF_2$ detector [19, 21, 22]. It appeared that this uncertainty was mainly determined by the difference in binding energy of sample and standard, which is large for the odd, but small for the even gadolinium isotopes. For neodymium, this difference is about equal for all isotopes, but with different sign for the odd and even nuclei. Therefore, an uncertainty of 0.6% was assigned to all isotopes. The comparison between the exact calculation and the Monte Carlo simulation (Table 9) showed differences of only 0.4% for the even and 0.2% for the odd isotopes, on average. In future, it is, therefore, possible to rely on the Monte Carlo results without significantly increasing the uncertainties.

# 6 MAXWELLIAN AVERAGED CROSS SECTIONS

Maxwellian averaged cross sections were calculated in the same way as described in Refs. [21, 24]. The neutron energy range from 0 to 700 keV was divided into three intervals according to the origin of the adopted cross sections. The respective contributions $I_x$ are given in Table 23. The main contribution, i.e. the interval $I_2$ from 3 to 225 keV, is provided by the results of this experiment (Table 21) (except for $^{142}$Nd where the lower limit had to be raised to 5 keV). These data were obtained with sufficient resolution to exclude systematic uncertainties that may be caused by a coarse energy grid.

The contributions $I_1$ were determined in two different ways. First, the cross sections were calculated from resonance parameters [31] and normalized to the present data in the overlapping energy region. In a second calculation, the cross sections of the JEF file [27] were normalized to the present data between 5 to 20 keV, the respective normalization factors being close to unity for $^{142,143,145,146}$Nd but reaching values of 1.3 for $^{148}$Nd and even 2.0 for $^{144}$Nd. The normalization factors were very similar in both calculations since at low energies the JEF cross section are also mainly based on the experimental resonance parameters. The quoted cross section uncertainties of 10% in the interval $I_1$ include the respective systematic uncertainties.

The energy interval from 225 to 700 keV contributes very little to the Maxwellian average at typical s–process temperatures. Here we used the JEF data normalized to the present results in the energy range from 100 to 225 keV. The uncertainties of the normalized cross sections were assumed to increase from 2% at 225 keV to 10% at 700 keV neutron energy.

The systematic uncertainties of the Maxwellian averaged cross sections in Table 23 correspond to the uncertainties of the cross section ratios (Table 20) and consider the contributions of the summed intensities, $I_2 + I_3$. The 1.5% uncertainty of the gold standard was not included since it cancels out in most applications of relevance for s–process studies. In most cases, the final uncertainties are dominated by the systematic components, except for low stellar temperatures where statistical uncertainties become important as well.

The stellar cross sections for a thermal energy of kT=30 keV are listed in Table 24 with previous experiments and with the compilations of Bao and Käppeler [17] and of Beer, Voss, and Winters [40]. First, the comparison of the present results with the preliminary analysis [41] exhibits differences comparable to the quoted uncertainties in the final data. These differences are due to the following reasons:
(i) The final data are based on 4 runs, the preliminary values on the first two runs only.
(ii) The isotopic composition was redetermined after the experiment replacing the composition that was originally provided with the samples.
(iii) The isotopic correction for the $^{145}$Nd impurity in the $^{144}$Nd sample was renormalized

to avoid overcompensation.

Except for $^{142}$Nd and $^{144}$Nd all differences are marginal which confirms, that the counting statistics of two runs is sufficient to determine the cross sections at 30 keV. The larger difference for $^{142}$Nd of 2.1% results from the improvements with respect to isotopic composition (1.7%) and counting statistics (0.4%). Similarly, the 4.1% change of the $^{144}$Nd cross section is due to the new isotopic composition (1.5%), the renormalization of the $^{145}$Nd impurity (2.0%) and the better counting statistics (0.6%).

Compared to the final values of a recent experiment at ORNL by Guber et al. [42] good agreement is found for $^{142}$Nd, but for $^{144}$Nd there was better agreement with the preliminary value of these authors [43]. The present $^{146}$Nd and $^{148}$Nd cross sections show also good agreement with the results of a recent activation experiment by Toukan et al. [4]. However, severe discrepancies are observed with respect to the older data for all isotopes, reflecting the difficulties encountered in these Nd measurements. Since both compilations [17, 40] are based on the old data, they reflect these discrepancies as well. With the results of this work as well as those of Guber et al. [42] and Toukan et al. [4] the stellar cross section data for the neodymium isotopes are sufficiently well established for a quantitative discussion of the nucleosynthesis yields in this mass region.

At lower stellar temperatures, corresponding to thermal energies around 10 keV, the situation is less favorable. The present data differ by up to 6% from the results of the preliminary analysis [33] due to the improved counting statistis which are more important at lower energies. Larger discrepancies show up with respect to the data of Guber et al. [42], their final values being higher by 9% in case of $^{142}$Nd but lower by 25% in case of $^{144}$Nd.

Table 23: MAXWELLIAN AVERAGED NEUTRON CAPTURE CROSS SECTIONS OF THE NEODYMIUM ISOTOPES.

| $^{142}$Nd | | | | | | | |
|---|---|---|---|---|---|---|---|
| $\Delta$E | 0 - 5 keV | 5 - 225 keV | 225 - 700 keV | Thermal Spectrum | | | |
| Data: | see text | this work | from Ref.[27][1] | | | | |
| kT | $I_1$ | $I_2$ | $I_3$ | $<\sigma v>/v_T$ (mbarn) | | | |
| (keV) | (mb) | (mb) | (mb) | | stat | sys[2] | tot |
| 10 | 11.9±1.2 | 48.2±1.2 | 0.0 | 60.1 | 1.7 | 0.9 | 1.9 |
| 12 | 8.7±0.9 | 45.7±1.0 | 0.0 | 54.4 | 1.3 | 0.9 | 1.6 |
| 20 | 3.5±0.4 | 38.0±0.5 | 0.0 | 41.5 | 0.6 | 0.7 | 0.9 |
| 25 | 2.3±0.2 | 34.8±0.4 | 0.0 | 37.1 | 0.4 | 0.7 | 0.8 |
| 30 | 1.6±0.2 | 32.3±0.4 | 0.1 | 34.0 | 0.4 | 0.6 | 0.7 |
| 40 | 1.0±0.1 | 28.5±0.3 | 0.4 | 29.9 | 0.3 | 0.5 | 0.6 |
| 50 | 0.6±0.1 | 25.5±0.2 | 1.0 | 27.1 | 0.2 | 0.5 | 0.5 |
| 52 | 0.6±0.1 | 25.0±0.2 | 1.1 | 26.7 | 0.2 | 0.5 | 0.5 |
| 60 | 0.4±0.0 | 22.9±0.2 | 1.8±0.1 | 25.1 | 0.2 | 0.5 | 0.5 |
| 70 | 0.3±0.0 | 20.7±0.2 | 2.7±0.1 | 23.7 | 0.2 | 0.4 | 0.4 |
| 80 | 0.3±0.0 | 18.7±0.2 | 3.7±0.1 | 22.7 | 0.2 | 0.4 | 0.4 |
| 90 | 0.2±0.0 | 16.9±0.2 | 4.7±0.2 | 21.8 | 0.3 | 0.4 | 0.5 |
| 100 | 0.2±0.0 | 15.3±0.1 | 5.5±0.2 | 21.0 | 0.2 | 0.4 | 0.4 |
| $^{143}$Nd | | | | | | | |
| $\Delta$E | 0 - 3 keV | 3 - 225 keV | 225 - 700 keV | Thermal Spectrum | | | |
| Data: | see text | this work | from Ref.[27][1] | | | | |
| kT | $I_1$ | $I_2$ | $I_3$ | $<\sigma v>/v_T$ (mb) | | | |
| (keV) | (mb) | (mb) | (mb) | | stat | sys[2] | tot |
| 10 | 97.0±9.7 | 431.3±4.1 | 0.0 | 528.3 | 11. | 6.0 | 13. |
| 12 | 68.9±6.9 | 392.4±3.3 | 0.0 | 461.3 | 7.6 | 5.5 | 9.4 |
| 20 | 26.0±2.6 | 294.7±1.7 | 0.0 | 320.7 | 3.1 | 4.1 | 5.1 |
| 25 | 16.8±1.7 | 258.8±1.3 | 0.1 | 275.7 | 2.1 | 3.6 | 4.2 |
| 30 | 11.8±1.2 | 232.4±1.1 | 0.4 | 244.6 | 1.6 | 3.3 | 3.7 |
| 40 | 6.7±0.7 | 195.2±0.8 | 2.0±0.1 | 203.9 | 1.1 | 2.8 | 3.0 |
| 50 | 4.3±0.4 | 169.0±0.7 | 5.1±0.2 | 178.4 | 0.8 | 2.4 | 2.5 |
| 52 | 4.0±0.4 | 164.5±0.7 | 5.8±0.2 | 174.3 | 0.8 | 2.4 | 2.5 |
| 60 | 3.0±0.3 | 148.4±0.6 | 9.2±0.3 | 160.6 | 0.7 | 2.2 | 2.3 |
| 70 | 2.2±0.2 | 131.5±0.5 | 13.9±0.5 | 147.6 | 0.7 | 2.0 | 2.1 |
| 80 | 1.7±0.2 | 117.2±0.5 | 18.6±0.7 | 137.5 | 0.9 | 1.9 | 2.1 |
| 90 | 1.4±0.1 | 105.1±0.4 | 23.1±0.9 | 129.6 | 1.0 | 1.8 | 2.1 |
| 100 | 1.1±0.1 | 94.6±0.4 | 27.2±1.1 | 122.9 | 1.2 | 1.7 | 2.1 |

TABLE 23 (continued)

| $^{144}$Nd | | | | | | | |
|---|---|---|---|---|---|---|---|
| $\Delta$E | 0 - 3 keV | 3 - 225 keV | 225 - 700 keV | Thermal Spectrum | | | |
| Data: | see text | this work | from Ref.[27][1] | | | | |
| kT | $I_1$ | $I_2$ | $I_3$ | $<\sigma v>/v_T$ (mb) | | | |
| (keV) | (mb) | (mb) | (mb) | | stat | sys[2] | tot |
| 10 | 29.3±2.9 | 123.8±2.8 | 0.0 | 153.1 | 4.0 | 2.1 | 4.5 |
| 12 | 20.9±2.1 | 114.9±2.1 | 0.0 | 135.8 | 3.0 | 2.0 | 3.6 |
| 20 | 7.9±0.8 | 92.8±1.0 | 0.0 | 100.7 | 1.3 | 1.6 | 2.1 |
| 25 | 5.1±0.5 | 84.5±0.7 | 0.0 | 89.6 | 0.9 | 1.4 | 1.7 |
| 30 | 3.6±0.4 | 78.3±0.6 | 0.2 | 82.1 | 0.7 | 1.3 | 1.5 |
| 40 | 2.0±0.2 | 68.9±0.4 | 0.9 | 71.8 | 0.4 | 1.2 | 1.3 |
| 50 | 1.3±0.1 | 61.6±0.3 | 2.3±0.1 | 65.2 | 0.3 | 1.1 | 1.1 |
| 52 | 1.2±0.1 | 60.3±0.3 | 2.7±0.1 | 64.2 | 0.3 | 1.1 | 1.1 |
| 60 | 0.9±0.1 | 55.4±0.3 | 4.3±0.1 | 60.6 | 0.3 | 1.0 | 1.0 |
| 70 | 0.7±0.1 | 49.9±0.3 | 6.5±0.2 | 57.1 | 0.4 | 1.0 | 1.1 |
| 80 | 0.5±0.1 | 45.1±0.2 | 8.8±0.3 | 54.4 | 0.4 | 0.9 | 1.0 |
| 90 | 0.4±0.0 | 40.8±0.2 | 11.0±0.4 | 52.2 | 0.4 | 0.9 | 1.0 |
| 100 | 0.3±0.0 | 37.0±0.2 | 13.1±0.5 | 50.4 | 0.5 | 0.9 | 1.0 |
| $^{145}$Nd | | | | | | | |
| $\Delta$E | 0 - 3 keV | 3 - 225 keV | 225 - 700 keV | Thermal Spectrum | | | |
| Data: | see text | this work | from Ref.[27][1] | | | | |
| kT | $I_1$ | $I_2$ | $I_3$ | $<\sigma v>/v_T$ (mb) | | | |
| (keV) | (mb) | (mb) | (mb) | | stat | sys[2] | tot |
| 10 | 146.9±15. | 748.3±5.7 | 0.0 | 895.2 | 16. | 9.7 | 19. |
| 12 | 104.8±10. | 683.8±4.6 | 0.0 | 788.6 | 11. | 8.9 | 14. |
| 20 | 39.8±4.0 | 517.3±2.5 | 0.0 | 557.1 | 4.7 | 6.7 | 8.2 |
| 25 | 25.9±2.6 | 453.7±2.0 | 0.2 | 479.8 | 3.3 | 5.9 | 6.8 |
| 30 | 18.2±1.8 | 406.0±1.7 | 0.6 | 424.8 | 2.5 | 5.3 | 5.9 |
| 40 | 10.3±1.0 | 337.7±1.3 | 3.0±0.1 | 351.0 | 1.6 | 4.4 | 4.7 |
| 50 | 6.7±0.7 | 289.2±1.1 | 7.6±0.2 | 303.5 | 1.3 | 3.9 | 4.1 |
| 52 | 6.2±0.6 | 280.9±1.0 | 8.8±0.3 | 295.9 | 1.2 | 3.8 | 4.0 |
| 60 | 4.7±0.5 | 251.6±0.9 | 13.9±0.4 | 270.2 | 1.1 | 3.5 | 3.7 |
| 70 | 3.4±0.3 | 221.2±0.8 | 20.9±0.7 | 245.5 | 1.1 | 3.1 | 3.3 |
| 80 | 2.6±0.3 | 196.0±0.8 | 28.0±1.0 | 226.6 | 1.3 | 2.9 | 3.2 |
| 90 | 2.1±0.2 | 174.7±0.7 | 34.8±1.3 | 211.6 | 1.5 | 2.7 | 3.1 |
| 100 | 1.7±0.2 | 156.6±0.6 | 40.9±1.6 | 199.2 | 1.7 | 2.6 | 3.1 |

TABLE 23 (continued)

| $^{146}$Nd | | | | | | | |
|---|---|---|---|---|---|---|---|
| ΔE | 0 - 3 keV | 3 - 225 keV | 225 - 700 keV | Thermal Spectrum | | | |
| Data: | see text | this work | from Ref.[27][1] | | | | |
| kT | $I_1$ | $I_2$ | $I_3$ | $<\sigma v>/v_T$ (mb) | | | |
| (keV) | (mb) | (mb) | (mb) | | stat | sys[2] | tot |
| 10 | 17.7±1.8 | 129.4±3.1 | 0.0 | 147.1 | 3.6 | 1.8 | 4.0 |
| 12 | 12.6±1.3 | 122.1±2.3 | 0.0 | 134.7 | 2.6 | 1.7 | 3.1 |
| 20 | 4.8±0.5 | 102.6±1.1 | 0.0 | 107.4 | 1.2 | 1.4 | 1.8 |
| 25 | 3.1±0.3 | 94.8±0.8 | 0.1 | 98.0 | 0.9 | 1.3 | 1.6 |
| 30 | 2.2±0.2 | 88.8±0.6 | 0.2 | 91.2 | 0.6 | 1.2 | 1.3 |
| 40 | 1.3±0.1 | 79.6±0.5 | 1.2 | 82.1 | 0.5 | 1.1 | 1.2 |
| 50 | 0.8±0.1 | 72.1±0.4 | 3.1±0.1 | 76.0 | 0.4 | 1.1 | 1.2 |
| 52 | 0.8±0.1 | 70.7±0.4 | 3.6±0.1 | 75.1 | 0.4 | 1.0 | 1.1 |
| 60 | 0.6±0.1 | 65.4±0.3 | 5.7±0.2 | 71.7 | 0.4 | 1.0 | 1.1 |
| 70 | 0.4±0.0 | 59.3±0.3 | 8.5±0.3 | 68.2 | 0.4 | 0.9 | 1.0 |
| 80 | 0.3±0.0 | 53.9±0.3 | 11.4±0.4 | 65.6 | 0.5 | 0.9 | 1.0 |
| 90 | 0.3±0.0 | 49.0±0.2 | 14.1±0.5 | 63.4 | 0.5 | 0.9 | 1.0 |
| 100 | 0.2±0.0 | 44.6±0.2 | 16.5±0.6 | 61.3 | 0.6 | 0.9 | 1.1 |
| $^{148}$Nd | | | | | | | |
| ΔE | 0 - 3 keV | 3 - 225 keV | 225 - 700 keV | Thermal Spectrum | | | |
| Data: | see text | this work | from Ref.[27][1] | | | | |
| kT | $I_1$ | $I_2$ | $I_3$ | $<\sigma v>/v_T$ (mb) | | | |
| (keV) | (mb) | (mb) | (mb) | | stat | sys[2] | tot |
| 10 | 53.0±5.4 | 212.8±3.4 | 0.0 | 265.8 | 6.4 | 3.2 | 7.2 |
| 12 | 37.7±3.8 | 198.9±2.6 | 0.0 | 236.6 | 4.6 | 3.0 | 5.5 |
| 20 | 14.2±1.4 | 163.0±1.3 | 0.0 | 177.2 | 1.9 | 2.5 | 3.1 |
| 25 | 9.3±0.9 | 149.6±0.9 | 0.1 | 159.0 | 1.3 | 2.3 | 2.6 |
| 30 | 6.5±0.7 | 139.7±0.7 | 0.4 | 146.6 | 1.0 | 2.1 | 2.3 |
| 40 | 3.6±0.4 | 124.8±0.5 | 1.9±0.1 | 130.3 | 0.6 | 1.9 | 2.0 |
| 50 | 2.4±0.2 | 112.9±0.5 | 4.6±0.1 | 119.9 | 0.5 | 1.8 | 1.9 |
| 52 | 2.2±0.2 | 110.8±0.4 | 5.3±0.2 | 118.3 | 0.5 | 1.8 | 1.9 |
| 60 | 1.7±0.2 | 102.5±0.4 | 8.3±0.3 | 112.5 | 0.5 | 1.7 | 1.8 |
| 70 | 1.2±0.1 | 93.0±0.4 | 12.1±0.4 | 106.3 | 0.6 | 1.6 | 1.7 |
| 80 | 1.0±0.1 | 84.4±0.3 | 15.9±0.5 | 101.3 | 0.6 | 1.5 | 1.6 |
| 90 | 0.8±0.1 | 76.7±0.3 | 19.2±0.7 | 96.7 | 0.8 | 1.5 | 1.7 |
| 100 | 0.6±0.1 | 69.9±0.3 | 22.2±0.8 | 92.7 | 0.9 | 1.4 | 1.7 |

[1]normalized to present data

[2]The 1.5% uncertainty of the gold standard is not included, since it cancels out in most applications of relevance for nuclear astrophysics

Table 24: MAXWELLIAN AVERAGED CROSS SECTIONS AT kT=30 keV COMPARED TO PREVIOUS EXPERIMENTS AND EVALUATIONS

| Isotope | Evaluation | | Experiment | |
|---|---|---|---|---|
| | Ref. [17] | Ref. [40] | Cross section (mb) | Reference |
| $^{142}$Nd | 46± 4 | 46± 4 | 34.0 ± 0.7 | present work[1] |
| | | | 33.3 | Wisshak et al. (prel.) [41] |
| | | | 36.6 ± 3.0 | Guber et al. [42] |
| | | | 45.8 ± 1.7 | Guber et al. (prel.) [43] |
| | | | 46.8 ± 3.8 | Mathews et al. [9] |
| | | | 55 ± 7 | Musgrove et al. [44] |
| | | | 43 ± 7 | Kononov et al. [45] |
| $^{143}$Nd | 242± 10 | 242± 10 | 244.6 ± 3.7 | present work[1] |
| | | | 244 | Wisshak et al. (prel.) [41] |
| | | | 247 ± 11 | Mathews et al. [9] |
| | | | 319 ± 26 | Nakajima et al. [46] |
| | | | 252 ± 50 | Musgrove et al. [44] |
| | | | 243 | Kikuchi et al. [47] |
| $^{144}$Nd | 110 ± 6 | 108 ± 6 | 82.1 ± 1.5 | present work[1] |
| | | | 78.9 | Wisshak et al. (prel.) [33] |
| | | | 73.2 ± 6.1 | Guber et al. [42] |
| | | | 83.9 ± 2.5 | Guber et al.prel. [43] |
| | | | 114 ± 6 | Mathews et al.[9] |
| | | | 82 ± 17 | Kononov et al.[45] |
| | | | 63 ± 10 | Musgrove et al.[44] |
| | | | 76.8 | Kikuchi et al.[47] |
| $^{145}$Nd | 485±100 | 485 ± 10 | 424.8 ± 5.9 | present work[1]0 |
| | | | 422 | Wisshak et al. (prel.) [41] |
| | | | 380 ± 90 | Musgrove et al. [44] |
| | | | 623 ± 54 | Nakajima et al. [46] |
| | | | 451 ± 45 | Shaw et al. [48] |
| | | | 300 | Kikuchi et al. [47] |
| $^{146}$Nd | 157 ± 40 | 157 ± 40 | 91.2 ± 1.3 | present work[1] |
| | | | 90 | Wisshak et al. (prel.) [41] |
| | | | 87.1 ± 4.0 | Toukan et al. [4] |
| | | | 80 ± 7 | Bradley et al. [49] |
| | | | 190 ± 19 | Kononov et al. [45] |
| | | | 113 ± 25 | Musgrove et al. [44] |
| | | | 152 ± 54 | Nakajima et al. [46] |
| | | | 102 ± 16 | Siddappa et al. [50] |
| | | | 52 ± 19 | Thirumala et al. [51] |

TABLE 24 (continued)

| Isotope | Evaluation | | Experiment | |
|---|---|---|---|---|
| | Ref. [17] | Ref. [40] | Cross section (mb) | Reference |
| $^{148}$Nd | 192 ± 40 | 192 ± 40 | 146.6 ± 2.3 | present work[1] |
| | | | 148 | Wisshak et al. (prel.) [41] |
| | | | 152 ± 9 | Toukan et al. [4] |
| | | | 106 ± 15 | Bradley et al. [49] |
| | | | 135 ± 15 | Iijima et al. [52] |
| | | | 208 ± 26 | Nakajima et al. [46] |
| | | | 172 ± 18 | Kononov et al. [45] |
| | | | 123 ± 20 | Musgrove et al. [44] |
| | | | 192 ± 35 | Siddappa et al. [50] |
| | | | 296 ± 120 | Thirumala et al. [51] |

[1] The 1.5% uncertainty of the gold cross section is not included, since it cancels out in most applications of relevance for nuclear astrophysics.

# 7 ASTROPHYSICAL IMPLICATIONS

## 7.1 The Nd Branchings in the reaction path of the s-Process

The neutron capture flow through the neodymium isotopes is characterized by the s–process branchings at A=141/142 and at A=147/148/149. The latter branching, which is suited for determining the neutron density, is practically not affected by the present results due to the very good agreement with the $^{146}$Nd and $^{148}$Nd cross sections obtained for the previous analysis (see Table24) [4]. In this case the more accurate data of this work yield an improved decomposition of the observed abundances into their respective s- and r-process components (see below). For the analysis of the branchings at $^{141}$Ce and $^{142}$Pr, the new data represent the relevant information that was missing in a recent study of the stellar (n,$\gamma$) rates of the Ce and Pr isotopes [2].

The present analysis follows the prescription given in Ref. [2], but complementing the previously used set of Maxwellian averaged cross sections by the new values for the Nd isotopes as well as by the preliminary cross section of $^{141}$Pr (108±2.5 mbarn at kT=30 keV) that has recently been measured with the Karlsruhe 4$\pi$ $BaF_2$ detector [53]. As before, two models were employed in this analysis, the classical approach representing a purely empirical treatment of the s–process [1], and a stellar model associated with helium shell burning in low mass stars [54, 55, 56].

The classical steady s–process model [57, 58, 59] with the extension for the treatment of branchings in the reaction path [60] has long been considered a useful tool for describing the s–process abundances, but also for estimating the physical conditions during the s–process via the abundance patterns of the various branchings. A detailed description of the basic features and of the formalism may be found in Refs. [1, 21].

Table 25: ABUNDANCE CONTRIBUTIONS FROM THE s–, AND r–PROCESSES TO THE MASS REGION BETWEEN $^{140}$Ce AND $^{148}$Nd

| Isotope | Solar Abundance[1] | Classical approach[2] | | | Stellar model[2,3] |
|---|---|---|---|---|---|
| | $N_\odot \times 10^2$ | $<\sigma>N_s$ | $N_s \times 10^2$ | $N_r \times 10^2$ | $N_s \times 10^2$ |
| $^{140}$Ce | 100.5±1.7 | 10.29 | 91.8±3.9 | 8.9±4.2 | 85.7 |
| $^{141}$Pr | 16.7±0.40 | 9.611 | (9.13±0.20)[4] | 7.6±0.5 | 7.51[4] |
| $^{142}$Ce | 12.6±0.21 | 0.326 | 1.13±0.04 | 11.3±0.21 | 1.62 |
| $^{142}$Nd | 22.5±0.29 | 8.696 | **(25.2±0.6)**[4,5] | ... | 22.3[4] |
| $^{143}$Nd | 10.0±0.13 | 8.994 | (3.62±0.08)[4] | 6.50±0.15 | 3.23[4] |
| $^{144}$Nd | 19.7±0.26 | 8.648 | 10.36±0.23 | 9.34±0.35 | 10.1 |
| $^{145}$Nd | 6.87±0.09 | 8.580 | 1.99±0.04 | 4.88±0.10 | 1.91 |
| $^{146}$Nd | 14.2±0.18 | 8.273 | 8.92±0.19 | 5.28±0.22 | 9.17 |
| $^{148}$Nd | 4.77±0.06 | 0.555 | 0.367±0.008 | 4.40±0.06 | 0.67 |

[1] From Ref. [63].
[2] Normalized at $^{150}$Sm.
[3] from Gallino and Arlandini [61].
[4] Including the decay of isobars.
[5] **12 % OVERPRODUCTION!**

In the following analysis, the s–process reaction flow was followed as indicated by the solid lines in Fig. 1 using an exponential distribution of neutron exposures, $\rho(\tau) \sim \exp(-\tau/\tau_0)$, suited for describing the s–abundances of the main component, i.e. between Zr and Pb [1]. The parameters for this calculation were an effective thermal energy kT = 29 keV [62], a mean exposure $\tau_0$=0.295 mb$^{-1}$ for kT=29 keV, and a mean neutron density of $n_n = (4.1 \pm 0.6) \times 10^8$ cm$^{-3}$ [4].

The s–abundances obtained from the classical approach are listed in Table 25. The $\langle\sigma\rangle N_s$-values are normalized to the nearby s-only isotope $^{150}$Sm, and carry, therefore, a 1.6% uncertainty due to the respective uncertainties of the samarium abundance (1.3%) and of the $^{150}$Sm cross section (0.9%). The Ce/Pr part of this table exhibits only modest changes compared to the corresponding table in Ref. [2] due to the new $^{141}$Pr cross section. In the lower part of Table 25, however, the new Nd data - and the $^{142}$Nd cross section in particular - are giving rise to significant changes. The most remarkable difference is that the classical model yields an unavoidable overproduction of $^{142}$Nd compared to the solar abundance despite the branchings at A=141/142 cause part of the reaction flow to bypass this isotope. Before, the s-abundance of $^{142}$Nd accounted only for 80% of the solar value due to the overestimated cross section.

Obviously, the calculated overproduction of 12% represents a lower limit, since the solar value may contain a certain abundance contribution from the p-process as well. But in view of the 2% uncertainty of the measured cross section, even this lower limit is completely sufficient to represent the first convincing inherent inconsistency of the classical model. With respect to this problem it can not be argued (as in the similar studies on Ba [19] and Sn [28]) that the calculated excess may be accounted for by the uncertainty of

the elemental abundance. For $^{142}$Nd, this possibility is completely excluded because the calculation is normalized at $^{150}$Sm, the relative abundance ratio being known to 1.8% [63] for these chemically related rare earth elements.

This failure of the classical model in reproducing the $^{142}$Nd abundance is certainly a clear hint that the simple assumptions of this approach are not adequate for describing the true stellar scenario. Though the classical model may still be a useful approximation, this is now the point to accept that a realistic, modern description of the s-process must be based on stellar models for the He burning phase.

Current stellar scenarios for the s-process are the helium shell burning episodes in low mass AGB stars, which have been shown to reproduce the *main* s–process component to better than 10% [56, 62, 64]. Contrary to the classical picture, this model is characterized by two neutron sources. Most of the neutron exposure is provided by the $^{13}$C($\alpha$,n)$^{16}$O reaction at comparably low neutron densities and temperatures. The resulting abundance distribution is modified by a second neutron burst, when the $^{22}$Ne($\alpha$,n)$^{25}$Mg reaction is activated at the higher temperatures towards the end of the helium–burning episode, mostly affecting the isotope patterns in the s-process branchings. Accordingly, these alternating neutron sources are characterized by a complex time dependence of neutron density, temperature, and mass density.

This model was used in the updated version of Straniero *et al.* [65], where the $^{13}$C($\alpha$,n)$^{16}$O reaction burns already at the low temperatures between the actual He shell flashes. This means that the neutron density during this exposure is always below $10^7$ cm$^{-3}$, resulting in a significantly smaller $^{142}$Ce production. The subsequent neutron exposure at the higher temperature of the the $^{22}$Ne phase is too small to restore that branching completely because of the relatively small cross sections involved.

The s-abundances obtained with this stellar model are listed in column 6 of Table 25. The most important difference compared to the classical approach refers to $^{142}$Nd, which is perfectly reproduced. Even the expected p-component can be accomodated within the typical uncertainty of a few percent. A detailed discussion of this result and of the consequences for the Sn and Ba problem is presently being prepared [66].

## 7.2 Isotopic anomalies

The overproduction of $^{142}$Nd by the classical model affects also the interpretation of the isotopic anomalies that have been discovered in meteoritic neodymium, first in acid resistant residues of the Allende meteorite [67] and - much more pronounced - in silicon carbide grains from the Murchison meteorite [14, 15, 68]. These anomalies were interpreted as being due to s–process Nd [69], but the anomalous isotopic pattern [68],

$^{142}$Nd/$^{143}$Nd/$^{144}$Nd/$^{145}$Nd/$^{146}$Nd/$^{148}$Nd/$^{150}$Nd =

$$2.13\pm0.08/0.293\pm0.006/\equiv1/0.161\pm0.005/0.775\pm0.009/0.0281\pm0.0058/\equiv0$$

showed large discrepancies with the s-process abundances obtained with the Nd cross sections existing at that time. With the s–abundances obtained in this work,

$$2.43\pm0.08/0.35\pm0.01/\equiv1/0.19\pm0.01/0.86\pm0.03/0.035\pm0.001/\equiv0.$$

the anomaly can be much better described, except for the significant difference at the overproduced $^{142}$Nd. If this s-abundance is replaced by the solar value, there is almost perfect agreement with the meteoritic pattern. Figure 18 summarizes the situation for the

classical approach. While the uncertainties of the present data points are smaller than the size of the symbols, the corresponding results obtained with the recently reported cross sections for $^{142}$Nd and $^{144}$Nd by Guber *et al.* [42] are less significant due to their larger uncertainties. On the other hand, the smaller $^{144}$Nd cross section of Ref. [42] leads to a better overall agreement with the measured anomaly, though the error bars are always compatible with the present results.

The interpretation of the isotopic anomalies in SiC grains via the stellar model showed that this material was produced in AGB stars of about solar metallicity, whereas the average s-process distribution in the interstellar medium – i.e. the *main* component – at that epoch originated from previous stellar generations with lower metallicity [64, 70]. However, this difference is not significant with respect to the Nd anomaly as can be seen from the comparison in Fig. 18, where the crosses denote the results of the stellar model for the *main* component case included in Table 25 while the standard case for describing the SiC patterns [70] is indicated by stars.

Though the latter calculation was using the cross sections of Guber *et al.* [42] for $^{142}$Nd and $^{144}$Nd and all the other Nd cross sections from the present work, there is rather good agreement with the pattern calculated via the classical approach, except for the striking discrepancy at A=148. The respective model predictions exceed the observed $^{148}$Nd anomaly by 6 and 4 standard deviations for the *main* component (crosses) and the SiC pattern (stars), if the small influence of the cross section uncertainties is neglected compared to the 20% uncertainty of the meteoritic abundance ratio. This difference is obviously due to an overestimation of the neutron capture part at the branch point $^{147}$Nd. Accordingly, the stellar s-abundance of $^{142}$Ce in Table 25 is also larger than predicted by the classical approach, indicating a similar effect for the branching at A=141. This overestimation of the neutron capture part at A=141 and 147 is interesting since the majority of the branchings is properly reproduced by the stellar model [61]. In particular one finds that the abundance ratio of the critical s-only isotopes $^{148}$Sm and $^{150}$Sm is correctly described [70]. Therefore, it might be worth while to check whether this difficulty is accounted for by a possible range od stellar masses and metallicities.

## 7.3 r–and p–process abundances

The cross sections determined in this work were also used to update the r–process residuals, $N_r$=$N_\odot$–$N_s$, in the mass range 140 < A < 146 (Table 25), which contribute to a better characterization of the r–process abundance peak at A = 130 as shown in Fig. 19. Open symbols denote the r–process yields for even and odd mass numbers of Käppeler *et al.* [1] updated by the recent studies in Refs. [2, 4, 19, 20, 71]. Though the new cross section of $^{144}$Nd led to a significant reduction of the corresponding r-component, the values at A=142 and 144 are still somewhat higher than a smooth interpolation of the general r–process pattern for the even isotopes in this region.

For $^{142}$Nd, the previously noted difference $N_\odot$ – $N_s$ = 0.041±0.016, corresponding to a p-process contribution of 18% [2] does no longer exist in view of the unacceptable overproduction by the classical s-process. The first results with the stellar model are - at least if the respective uncertainties are considered - compatible with the 4% contribution obtained in recent p-process calculations [6, 72, 73].

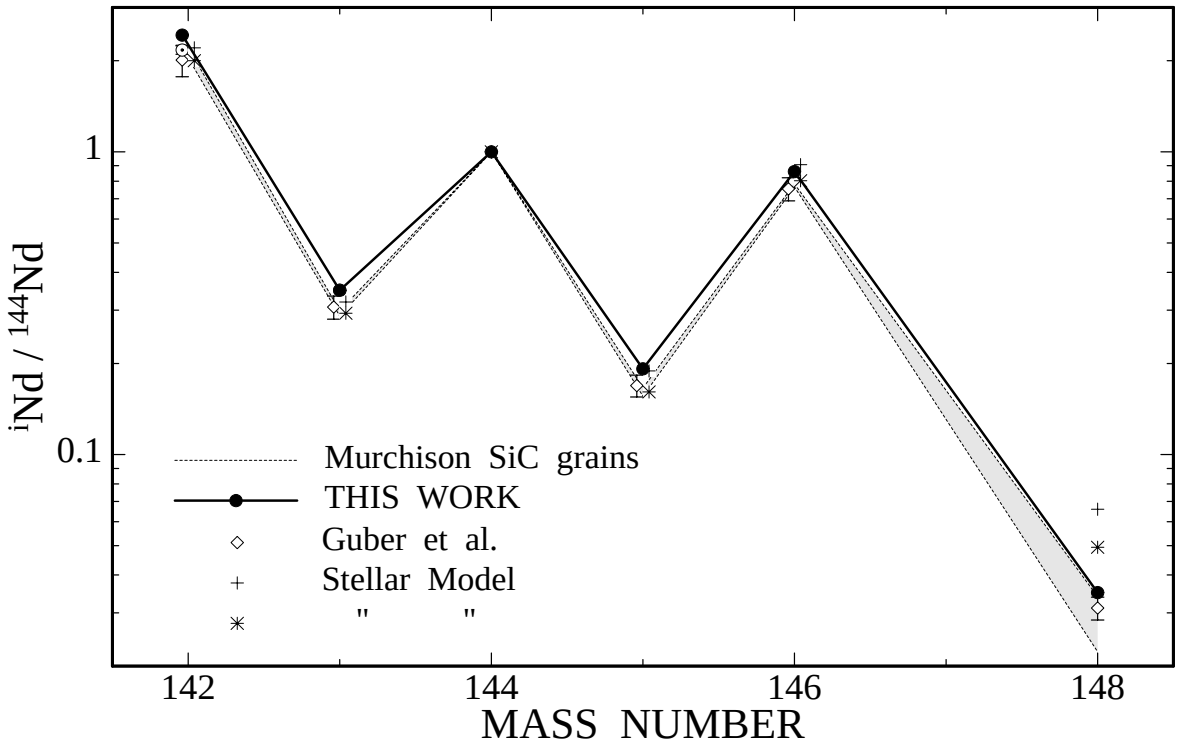


Figure 18: Comparison of s–process neodymium (this work) with the anomalous abundance pattern reported for SiC inclusions in the Murchison meteorite [14] (shaded area). The results of Guber *et al.* [42] and from recent stellar model calculations for the *main* component (+) [61] and the more suited description of the anomalies in meteoritic SiC grains (*) [70] are included as well.

Summation of the isotopic abundances in Table 25 yields an r-process component of 42±1% for the elemental Nd abundance if the small p-component is neglected. This result is significantly smaller than the 51% obtained with the previous Nd cross sections [1]. Along with the observed variation in the ratio of r-process abundances to s-process abundances over time in the Galaxy [13], this revised s/r–ratio of the solar Nd components is important with respect to a future update of the Th/Nd chronometer suggested by Butcher [12]. In this context it is worth noting that the 20% reduction in the r-component of elemental neodymium is in perfect agreement with the observations of Woolf *et al.* [13] who found a 0.06 dex or 15% difference compared to the s-process yields of Howard *et al.* [74] which were also based on the old cross sections.

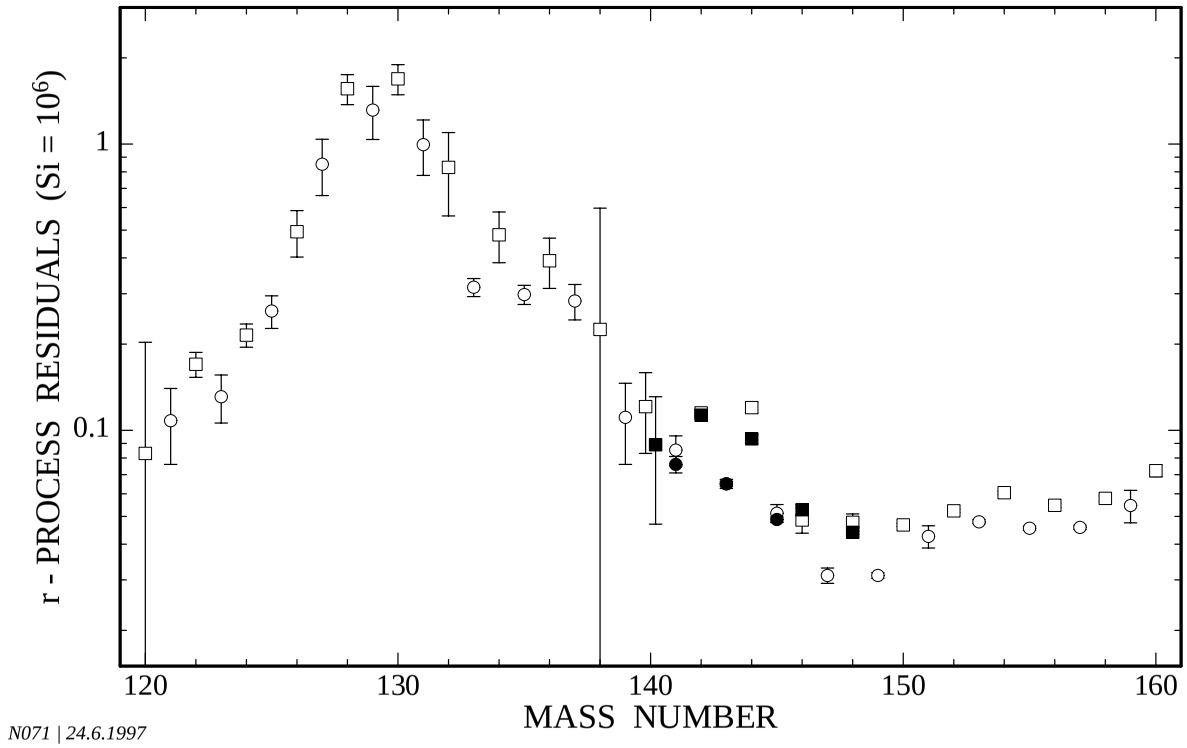


Figure 19: The r–process abundance peak at mass number A=130. Values from the present analysis are indicated by black symbols, open symbols refer to the results of Ref. [2] (see text).

# 8 ACKNOWLEDGMENTS

We would like to thank F.H. Fröhner and B. Krieg for providing us with the JEF data as well as C. Arlandini and R. Gallino for the information concerning the s-process yields from their stellar model. We are indebted to H. Kohl and A. Stollenwerk for their isotope analyses of the sample material. Our special thanks go to G. Rupp for his skilful and permanent help in optimizing the experimental setup. The continuous support by D. Roller, E.–P. Knaetsch, and W. Seith, who ran the accelerator in a most efficient way, is also greatly appreciated.

# References


[1] F. Käppeler, H. Beer, and K. Wisshak, Rep. Prog. Phys. **52**, 945 (1989).

[2] F. Käppeler, K.A. Toukan, M. Schumann, and A. Mengoni, Phys. Rev. C **53**, 1397 (1996).

[3] K. Takahashi and K. Yokoi, Atomic Data Nucl. Data Tables **36**, 375 (1987).

[4] K.A. Toukan, K. Debus, F. Käppeler, and G. Reffo, Phys. Rev. C **51**, 1540 (1995).

[5] M. Rayet, N. Prantzos, and M. Arnould, Astron. Astrophys. **227**, 271 (1990).

[6] M. Rayet, M. Arnould, M. Hashimoto, N. Prantzos, and K. Nomoto, Astron. Astrophys. **298**, 517 (1995).

[7] W.M. Howard, B.S. Meyer, and S.E. Woosley, Astrophys. J. **373**, L5 (1991).

[8] A. Prinzhofer, D.A. Papanastassiou, and G.J. Wasserburg, Astrophys. J. **344**, L81 (1989).

[9] G.J. Mathews and F. Käppeler, Astrophys. J. **286**, 810 (1984).

[10] B. Chen, J. Dobaczewski, K.–L. Kratz, K. Langanke, B. Pfeiffer, F.–K. Thielemann, and P. Vogel, Phys. Lett. B **355**, 37 (1995).

[11] B.S. Meyer, Astrophys. J. **449**, L55 (1995).

[12] H.R. Butcher, Nature **328**, 127 (1987).

[13] V.M. Woolf, J. Tomkin, and D.L. Lambert, Astrophys. J. **453**, 660 (1995).

[14] S. Richter, U. Ott, and F. Begemann, in Nuclei in the Cosmos, edited by F. Käppeler and K. Wisshak (IOP Publishing, Bristol, 1993), p. 127.

[15] E. Zinner, S. Amari, and R.S. Lewis, Astrophys. J. **382**, L47 (1991).

[16] R.Gallino, C.M. Raiteri, and M. Busso, Astrophys. J. **410**, 400 (1993).

[17] Z. Y. Bao and F. Käppeler, Atomic Data Nucl. Data Tables **36**, 411 (1987).

[18] Z. Y. Bao, private communications 1995.

[19] F. Voss, K. Wisshak, K. Guber, F.Käppeler, and G. Reffo, Phys. Rev. C **50**, 2582 (1994).

[20] K. Wisshak, F. Voss, F. Käppeler, K. Guber, L. Kazakov, N. Kornilov, M. Uhl, and G. Reffo, Phys. Rev. C. **52**, 2762 (1995).

[21] K. Wisshak, F. Voss, F. Käppeler, and G. Reffo, Phys. Rev. C **45**, 2470 (1992).

[22] K. Wisshak, K. Guber, F. Voss, F. Käppeler, and G. Reffo, Phys. Rev. C **48**, 1401 (1993).

[23] K. Wisshak, K. Guber, F. Käppeler, J. Krisch, H. Müller, G. Rupp, and F. Voss, Nucl. Instr. Meth. A **292**, 595 (1990).

[24] K. Wisshak, F. Voss, F. Käppeler, and G. Reffo, Phys. Rev. C **42**, 1731 (1990).

[25] M. Mizumoto and M. Sugimoto, Nucl. Instr. Meth. A **282**, 324 (1989).

[26] F. H. Fröhner, Technical report, Gulf General Atomic (unpublished).

[27] C. Nordborg, H. Gruppelaar, and M. Salvatores, in *Nuclear Data for Science and Technology*, edited by S. Qaim (Springer, Berlin, 1992), p. 782.

[28] K. Wisshak, F. Voss, Ch. Theis, F. Käppeler, K. Guber, L. Kazakov, N. Kornilov, and G. Reffo, Phys. Rev. C **54**, 1451 (1996).

[29] D.J. Horen, C.H. Johnson, J.L. Fowler, A.D. MacKellar, and B. Castel, Phys. Rev. C **34**, 429 (1986).

[30] K.K. Seth, Phys. Lett. **16**, 306 (1965).

[31] J. F. Mughabghab, M. Divadeenam, and N. E. Holden, in *Neutron Cross Sections, Vol. 1, Part A*, (Academic Press, New York, 1981).

[32] F. Voss, K. Wisshak, and F. Käppeler, Phys. Rev. C **52**, 1102 (1995).

[33] K. Wisshak, F. Voss, and F. Käppeler, Phys. Rev. C **54**, 2732 (1996).

[34] G. Reffo, F. Fabbri, K. Wisshak, and F. Käppeler, Nucl. Sci. Eng. **80**, 630 (1982).

[35] N. Weber, diplom thesis, University of Karlsruhe (1993).

[36] A. Gilbert and A.G.W. Cameron, Can. J. Phys. **43**, 1446 (1965).

[37] R. L. Macklin, private communication (unpublished).

[38] W. Ratynski and F. Käppeler, Phys. Rev. C **37**, 595 (1988).

[39] K. Wisshak, F. Voss, and F. Käppeler, report FZKA-5968, Forschungszentrum Karlsruhe 1997.

[40] H. Beer, F. Voss, and R.R. Winters, Astrophys. J. Suppl. **80**, 403 (1992).

[41] K. Wisshak, F. Voss, and F. Käppeler, in *Nuclei in the Cosmos 1996*, edited by J. Meissner and M. Wiescher, to appear as a volume of Nucl. Phys. (in press).

[42] K.H. Guber, R.R. Spencer, P.E. Koehler, and R.R. Winters, Phys. Rev. Lett. **78**, 2704 (1997).

[43] K.H. Guber, R.R. Spencer, P.E. Koehler, and R.R. Winters, in *Nuclei in the Cosmos 1996*, edited by J. Meissner and M. Wiescher, to appear as a volume of Nucl. Phys. (in press).

[44] A.R. de L. Musgrove, B.J. Allen, J.W. Boldeman, and R.L. Macklin, in *Proceedings of an Int. Conf. on Neutron Physics and Nuclear Data for Reactors and other Applied Purposes, Harwell, 1978*, (OECD, Paris 1978), p. 449.

[45] V.N. Kononov, B.D. Yurlov, E.D. Poletaev, and V.M. Timokhov, Yad. Fiz. **27**, 10 (1978).

[46] Y. Nakajima, A. Asami, Y. Kawarasaki, Y. Furuta, T. Yamamoto, and Y. Kanda, in *Proceedings of an Int. Conf. on Neutron Physics and Nuclear Data for Reactors and other Applied Purposes, Harwell, 1978*, (OECD, Paris 1978), p. 438.

[47] Y. Kikuchi, T. Nakagawa, H. Matsunobu, M. Kawai, S. Igarasi, and S. Iijima, Report JAERI-1268, NEANDC(J)–68/U, INDC (JAP)–55/L, Japan Atomic Research Institute, 1981.

[48] R.A. Shaw, W.R. Koste, and R.W. Hockenbury, Rensselaer Polytechnic Institute, Troy, New York, data communicated to the NEA Data Bank, Paris, 1975.

[49] T. Bradley, Z. Parsa, M.L. Stelts, and R.E. Chrien, in *Proc. of an Int. Conf. on Nuclear Cross Sections for Technology*, edited by J.L. Fowler, C.H. Johnson, and C.D. Bowman, Natl. Bur. Stand. (U.S.) Spec. Publ. No. 594 (U.S. GPO, Washington, D.C., 1979), p. 344.

[50] K. Siddappa, M. Sriramachandra Murty, and J. Rama Rao, Nuovo Cim. A **18** , 48 (1973).

[51] B.V. Thirumala Rao, J. Rama Rao, and E. Kondaiah, J. Phys. **A5**, 468 (1972).

[52] S. Iijima, T. Watanabe, T. Yoshida, Y. Kikuchi, and H. Nishimura, in *Neutron Cross Sections of Fission Product Nuclei*, edited by C. Coceva and G. Panini, Report RIT/FIS–LND(80) 1, NEANDC(E) 209"L", (C.N.E.N., Bologna, 1979), p. 317.

[53] K. Wisshak, F. Voss, F. Käppeler, and G. Reffo, in *Proc. of an Int. Conf. on Nuclear Data for Science and Technology*, edited by G. Reffo, A. Ventura, and C. Grandi (Springer, Berlin, 1997).

[54] I. Iben Jr. and A. Renzini, Ann. Rev. Astron. Astrophys. **21**, 271 (1983).

[55] D. Hollowell and I. Iben Jr., Astrophys. J. **340**, 966 (1989).

[56] R. Gallino, M. Busso, G. Picchio, C.M. Raiteri, and A. Renzini, Astrophys. J. **334**, L45 (1988).

[57] E. Burbidge, G. Burbidge, W. Fowler, and F. Hoyle, Rev. Mod. Phys. **29**, 547 (1957).

[58] P. Seeger, W. Fowler, and D. Clayton, Astrophys. J. Suppl. **97**, 121 (1965).

[59] D. Clayton and R. Ward, Astrophys. J. **193**, 397 (1974).

[60] R. Ward, M. Newman, and D. Clayton, Astrophys. J. Suppl. **31**, 33 (1976).

[61] R. Gallino and C. Arlandini, private communication (unpublished).

[62] F. Käppeler, R. Gallino, M. Busso, G. Picchio,and C.M.Raiteri, Astrophys. J. **354**, 630 (1990).

[63] E. Anders and N. Grevesse, Geochim. Cosmochim. Acta **53**, 197 (1989).

[64] R. Gallino, C.M. Raiteri, and M. Busso, Astrophys. J. **410**, 400 (1993).

[65] O. Straniero, R. Gallino, M. Busso, A. Chieffi, C.M. Raiteri, M. Limongi, and M. Salaris, Astrophys. J. **440**, L85 (1995).

[66] M. Busso, F. Käppeler, K. Wisshak, R. Gallino, M. Lugaro, C. Arlandini, and O. Straniero, in preparation (unpublished).

[67] G. Lugmair, T. Shimamura, R. Lewis, and E. Anders, Lunar Planet. Sci. **14**, 448 (1983).

[68] S. Richter, U. Ott, and F. Begemann, Lunar Planet. Sci. **23**, 1147 (1992).

[69] D. Clayton, Astrophys. J. **271**, L107 (1983).

[70] R. Gallino and M. Busso, in *Astrophysical Implications of the Laboratory Study of Presolar Materials*, edited by T.J. Bernatowicz, (American Institute of Physics, New York, 1997), in print.

[71] F. Käppeler, W. Schanz, K. Wisshak, and G. Reffo, Astrophys. J. **410**, 370 (1993).

[72] N. Prantzos, M. Hashimoto, M. Rayet, and M. Arnould, Astron. Astrophys. **238**, 455 (1990).

[73] M. Rayet, private communication (unpublished).

[74] W. Howard, W. Arnett, D. Clayton, and S. Woosley, Astrophys. J. **309**, 633 (1986).